The Astrophysical Journal, 856:125 (22pp), 2018 April 1 https://doi.org/10.3847/1538-4357/aab158

The Updated BaSTI Stellar Evolution Models and Isochrones. I. Solar-scaled Calculations

Sebastian L. Hidalgo[1,2], Adriano Pietrinferni[3], Santi Cassisi[3], Maurizio Salaris[4], Alessio Mucciarelli[5,6], Alessandro Savino[4,7], Antonio Aparicio[1,2], Victor Silva Aguirre[8], and Kuldeep Verma[8]
[1] Instituto de Astrofísica de Canarias, Via Lactea s/n, La Laguna, Tenerife, Spain; shidalgo@iac.es
[2] Department of Astrophysics, University of La Laguna, Via Lactea s/n, La Laguna, Tenerife, Spain
[3] INAF—Osservatorio Astronomico d'Abruzzo, Via M. Maggini, s/n, I-64100, Teramo, Italy
[4] Astrophysics Research Institute, Liverpool John Moores University, IC2, Liverpool Science Park, 146 Brownlow Hill, Liverpool, L3 5RF, UK
[5] Dipartimento di Fisica e Astronomia, Universitá degli Studi di Bologna, Via Piero Gobetti 93/2, I-40129, Bologna, Italy
[6] INAF—Osservatorio di Astrofisica e Scienza dello Spazio di Bologna, via Piero Gobetti 93/3—I-40129, Bologna, Italy
[7] Kapteyn Astronomical Institute, University of Groningen, Postbus 800, 9700 AV Groningen, The Netherlands
[8] Stellar Astrophysics Centre, Department of Physics and Astronomy, Aarhus University, Ny Munkegade 120, DK-8000 Aarhus C, Denmark
Received 2018 January 24; revised 2018 February 14; accepted 2018 February 19; published 2018 March 30

Abstract

We present an updated release of the BaSTI (a Bag of Stellar Tracks and Isochrones) stellar model and isochrone library for a solar-scaled heavy element distribution. The main input physics that have been changed from the previous BaSTI release include the solar metal mixture, electron conduction opacities, a few nuclear reaction rates, bolometric corrections, and the treatment of the overshooting efficiency for shrinking convective cores. The new model calculations cover a mass range between 0.1 and 15 $M_{\odot}$, 22 initial chemical compositions between [Fe/H] $= -3.20$ and $+0.45$, with helium to metal enrichment ratio $dY/dZ = 1.31$. The isochrones cover an age range between 20 Myr and 14.5 Gyr, consistently take into account the pre-main-sequence phase, and have been translated to a large number of popular photometric systems. Asteroseismic properties of the theoretical models have also been calculated. We compare our isochrones with results from independent databases and with several sets of observations to test the accuracy of the calculations. All stellar evolution tracks, asteroseismic properties, and isochrones are made available through a dedicated web site.

Key words: galaxies: stellar content – Galaxy: disk – open clusters and associations: general – stars: evolution – stars: general

1. Introduction

The interpretation of a vast array of astronomical observations, ranging from the photometry and spectroscopy of galaxies and star clusters, to individual single and binary stars, to the detection of exoplanets, requires accurate sets of stellar model calculations covering all major evolutionary stages and a wide range of masses and initial chemical compositions.

As just a few examples, the exploitation of the impressive amount of data provided by surveys like *Kepler* (Gilliland et al. 2010, asteroseismology), APOGEE and SAGA (Zasowski et al. 2013; Casagrande et al. 2014, Galactic archaeology), ELCID and ISLANDS (Gallart et al. 2015; Monelli et al. 2016, stellar population studies in resolved extragalactic stellar systems); present and future releases of the *Gaia* catalog (see, e.g., Gaia Collaboration et al. 2017); and observations with next-generation instruments like the *James Webb Space Telescope* and the Extremely Large Telescope all require the use of extended grids of stellar evolution models. In addition, the characterization of extrasolar planets in terms of their radii, masses, and ages (the main science goal, for example, of the future *PLATO* mission; see Rauer et al. 2016) is dependent on an accurate characterization of the host stars, which again requires the use of stellar evolution models.

In the last decade, several independent libraries of stellar models have been made available to the astronomical community, based on recent advances in stellar physics inputs like equations of state (EOS), Rosseland opacities, and nuclear reaction rates. Examples of these libraries are BaSTI (Pietrinferni et al. 2004, 2006, 2009), DSEP (Dotter et al. 2008), Victoria-Regina (see, VandenBerg et al. 2014, and references therein), Yale-Potsdam (Spada et al. 2017), PARSEC (Bressan et al. 2012; Chen et al. 2014), and MIST (Choi et al. 2016).

Our group has built and delivered to the scientific community the BaSTI (a Bag of Stellar Tracks and Isochrones) stellar model and isochrone library, which has been extensively used to study field stars, stellar clusters, and galaxies, both resolved and unresolved. In its first release, we delivered stellar models for a solar-scaled heavy element mixture (Pietrinferni et al. 2004), followed by complete sets of models for α-enhanced (Pietrinferni et al. 2006) and CNO-enhanced heavy element distributions (Pietrinferni et al. 2009). In Pietrinferni et al. (2013), we extended our calculations to the regime of extremely metal-poor and metal-rich chemical compositions. Extensions of the BaSTI evolutionary sequences to the final stages of the evolution of low- and intermediate-mass stars, i.e., the white dwarf cooling sequence and the AGB, were published in Salaris et al. (2010) and Cordier et al. (2007), while sets of integrated properties and spectra self-consistently based on the BaSTI stellar model predictions were provided in Percival et al. (2009).

Since the first release of BaSTI, several improvements of the stellar physics inputs have become available, together with a number of revisions of the solar metal distribution and corresponding revisions of the solar metallicity (e.g., Bergemann & Serenelli 2014 and references therein). We have therefore set out to build a new release of the BaSTI library including these revisions of physics inputs and solar metal mixtures, still ensuring that our models satisfy a host of empirical constraints. In addition—and this is entirely new compared to the previous BaSTI release—we

have also calculated and provided fundamental asteroseismic properties of the models.

This paper is the first one in a series that will present these new results. Here we focus on solar-scaled nonrotating stellar models, while in a forthcoming paper we will publish α-enhanced and α-depleted models. Metal mixtures appropriate to study the phenomenon of multiple populations in globular clusters (see Gratton et al. 2012; Cassisi & Salaris 2013; Piotto et al. 2015, and references therein) will be presented in future publications.

The plan of this paper is as follows. Section 2 details the physics inputs adopted in the new computations, including the new adopted solar-scaled heavy element distribution. Section 3 describes the standard solar model used to calibrate the mixing length and the He-enrichment ratio $\Delta Y/\Delta Z$, while Section 4 presents the stellar model grid, the mass and chemical composition parameter space covered, the adopted bolometric corrections (BCs), and the calculation of the asteroseismic properties of the models. Section 5 shows comparisons between our new models and recent independent calculations, while in Section 6, the models are tested against a number of observational benchmarks. Conclusions follow in Section 7.

2. Stellar Evolution Code, Solar Metal Distribution, and Physics Inputs

The evolutionary code[9] used in these calculations is the same one used to compute the original BaSTI library, albeit with several technical improvements to increase the model accuracy. For instance, we improved the mass layer (mesh) distribution and time-step determinations, to obtain more accurate physical and chemical profiles for asteroseismic pulsational analyses.

The treatment of the atomic diffusion of helium and metals has also been improved. We still include the effect of gravitational settling, and chemical and temperature gradients (no radiative levitation) following Thoul et al. (1994), but the numerical treatment has been improved to ensure smooth and accurate chemical profiles for all involved chemical species, from the stellar surface to the center. We have also eliminated the traditional Runge–Kutta integration of the more external sub-atmospheric layers using the pressure as an independent variable, with no energy generation equation and uniform chemical composition (equal to the composition of the outermost layers integrated with the Henyey method; see, e.g., Degl'Innocenti et al. 2008). Historically. this approach was chosen to save computing time, compared to a full Henyey integration up to the photosphere, with mass as an independent variable.

This separate integration of the sub-atmosphere, however, prevents a fully consistent evaluation of the effect of atomic diffusion, which is included in the Henyey integration only. Depending on the selected total mass of the sub-atmospheric layers, the effect of diffusion on the surface abundances of low-mass stars can be appreciably underestimated. In these new calculations, we have included the sub-atmosphere, consisting typically of $\sim$300 mass layers, in the Henyey integration. The more external mesh point contains typically mass of the order of $10^{-11} M_{\odot}$.

We have also performed tests to estimate the variation of the surface abundances of key elements when diffusion is treated with either pressure integration or Henyey mass integration of the sub-atmosphere. We fixed the total mass of the sub-atmospheric layers to 3.8×10^{-5} times the total mass of the model, as in the previous BaSTI release.

In the case of a $1M_{\odot}$ model with solar initial metallicity and helium mass fraction— $Z_{\odot}^{\rm ini} = 0.01721$, $Y_{\odot}^{\rm ini} = 0.2695$ (see Section 3)—at the main-sequence (MS) turnoff (approximately where the effect of diffusion is at its maximum), the surface mass fractions of He and Fe (representative of the metals) are essentially the same in both calculations. This is expected, given that the thickness of the sub-atmosphere is negligible compared to the total mass of the convective envelope. The case of lower metallicity low-mass models is different, with typically thinner (in mass) convective envelopes at the turnoff. A $0.8\,M_{\odot}$ model with initial $Z = 0.0001$ and $Y = 0.247$ displays an increase of the He and Fe mass fractions equal to 2% and 4%, respectively, at the turnoff, when the sub-atmosphere is included in the Henyey integration.

2.1. The Solar Heavy Element Distribution

The solar heavy element distribution sets the zero point of the metallicity scale and is also a critical input entering the calibration of the Solar Standard Model (SSM; Vinyoles et al. 2017), which in turn serves as a calibrator of the mixing-length parameter (see Section 2.7), the initial solar He abundance and metallicity, and the dY/dZ He-enrichment ratio.

"Classical" estimates of the solar heavy element distribution such as those by Grevesse & Sauval (1998) used in our previous BaSTI models did allow SSMs to match very closely the constraints provided by helioseismology (e.g., Pietrinferni et al. 2004 and references therein). Recent reassessments by Asplund et al. (2005, 2009) have led to a downward revision of the solar metal abundances by up to 40% for important elements such as oxygen. SSMs employing these new metal distributions produce a worse match to helioseismic constraints such as the sound speed at the bottom of the convective envelope, as well as the location of the bottom boundary of the surface convection and the surface He abundance (see, e.g., Serenelli et al. 2009). This evidence has raised the so-called "solar metallicity problem." A reanalysis of the Asplund et al. (2009) results and the use of an independent set of solar model atmospheres (see, e.g., Caffau et al. 2011 for a detailed discussion) has provided a solar heavy element distribution intermediate between those by Grevesse & Sauval (1998) and Asplund et al. (2009).

Although the problem is still unsettled and different solutions are under scrutiny (see, e.g., Vinyoles et al. 2017), we decided to adopt the solar metal mixture by Caffau et al. (2011), supplemented when necessary by the abundances given by Lodders (2010). The reference solar metal mixture adopted in our calculations is listed in Table 1. The actual solar metallicity is $Z_{\odot} = 0.0153$, while the corresponding actual $(Z/X)_{\odot}$ is equal to 0.0209.

2.2. The Treatment of Convective Mixing

In our models—apart from the case of core He burning in low- and intermediate-mass stars—we use the Schwarzschild criterion to fix the formal convective boundary, plus instantaneous mixing in the convective regions. In the case of models

[9] Starting from the work in preparation for the models published in Pietrinferni et al. (2004), we have adopted the acronym BaSTI to identify both our own calculations and the stellar evolution code employed for these computations. The code is an independent evolution of the FRANEC code described in Degl'Innocenti et al. (2008). The current version is denoted as BaSTI version 2.0.

Table 1
Abundances of the Most Relevant Heavy Elements in Our Adopted Solar Mixture

Element	Number Fraction	Mass Fraction
C	0.260408	0.180125
N	0.059656	0.048121
O	0.473865	0.436614
Ne	0.096751	0.112433
Na	0.001681	0.002226
Mg	0.029899	0.041850
Al	0.002487	0.003865
Si	0.029218	0.047258
P	0.000237	0.000423
S	0.011632	0.021476
Cl	0.000150	0.000306
Ar	0.002727	0.006274
K	0.000106	0.000239
Ca	0.001760	0.004063
Ti	0.000072	0.000199
Cr	0.000385	0.001153
Mn	0.000266	0.000842
Fe	0.027268	0.087698
Ni	0.001431	0.004838

of massive stars, where layers left behind by shrinking convective cores during the MS have a hydrogen abundance that increases with increasing radius, formally requiring a semiconvective treatment of mixing, we still use the Schwarzschild criterion and instantaneous mixing to determine the boundaries of the mixed region. This follows recent results from 3D hydrodynamic simulations of layered semiconvective regions (Wood et al. 2013) that show how in stellar conditions, mixing in MS semiconvective regions is very fast and essentially equivalent to calculations employing the Schwarzschild criterion and instantaneous mixing (Moore & Garaud 2016).

Theoretical simulations (see, e.g., Andrássy & Spruit 2013, 2015; Viallet et al. 2015 and references therein), observations of open clusters and eclipsing binaries (see, e.g., Demarque et al. 1994; Magic et al. 2010; Stancliffe et al. 2015; Claret & Torres 2016, 2017; Valle et al. 2016, and references therein), as well as asteroseismic constraints (see, e.g., Silva Aguirre et al. 2013) show that in real stars, chemical mixing beyond the formal convective boundary is required and most likely results from the interplay of several physical processes, grouped in stellar evolution modeling under the generic terms overshooting or convective boundary mixing.

In our calculations, overshooting beyond the Schwarzschild boundary of MS convective cores is included as an instantaneous mixing between the formal convective border and layers at a distance $\lambda_{ov}H_P$ from this boundary, keeping the radiative temperature gradient in this region. Here, H_P is the pressure scale height at the Schwarzschild boundary, and λ_{OV} a free parameter that we set equal to 0.2, decreasing to zero when the mass decreases below a certain value. This decrease is required because for increasingly small convective cores, the Schwarzschild boundary moves progressively closer to the center, and the local H_P increases quickly, formally diverging when the core shrinks to zero mass. Keeping λ_{OV} constant would produce increasingly large overshooting regions for shrinking convective cores.

How to decrease the overshooting efficiency is still somewhat arbitrary (see, e.g., Claret & Torres 2016; Salaris & Cassisi 2017 for a review of the different choices found in the literature). As shown by Pietrinferni et al. (2004), the approach used to decrease the overshooting efficiency in the critical mass range between ∼1.0 and ∼1.5 $M_\odot$ has a potentially large effect on the isochrone morphology for ages around ∼4–5 Gyr (see Figure 1 in Pietrinferni et al. 2004).

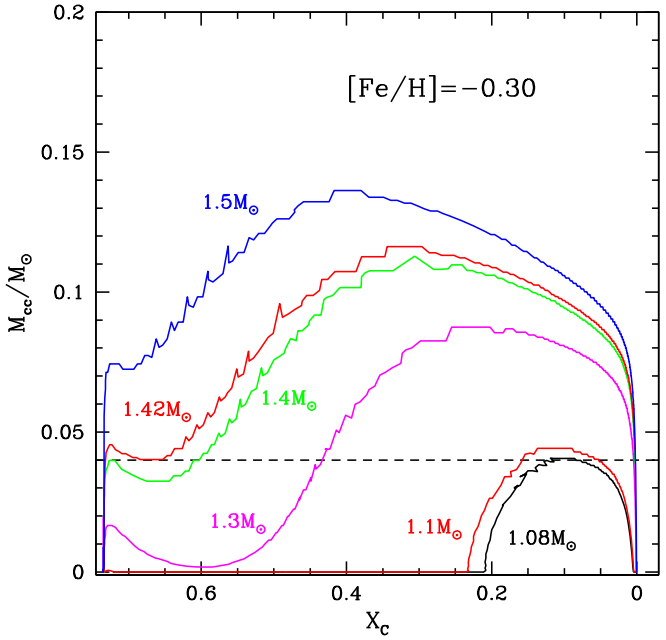

Figure 1. Convective core mass as a function of the central H mass fraction for stellar models with the labelled masses and a metallicity $Z = 0.0077$. The dashed line represents the value of M_{cc}^{min} adopted in our calculations. In this example, $M_{ov}^{inf} = 1.08\,M_\odot$ and $M_{ov}^{sup} = 1.42\,M_\odot$ (see text for details).

In these new calculations, we have chosen the following procedure to decrease λ_{OV} with decreasing initial mass of the model. For each chemical composition, we have sampled the mass range between $1.0 \leqslant M/M_\odot \leqslant 1.5$ with a very fine mass spacing, and determined the initial mass (M_{ov}^{inf}) that develops a convective core reaching, at its maximum extension, a mass $M_{cc}^{min} = 0.04\,M_\odot$ during core H burning. This initial mass is considered to be the maximum mass for models calculated with $\lambda_{OV} = 0$. We have then determined the minimum initial mass that develops a convective core that is always larger than M_{cc}^{min} during the entire MS. This value of the initial mass is denoted as M_{ov}^{sup}. For models with initial masses equal to or larger than M_{ov}^{sup}, we use $\lambda_{OV} = 0.2$, whereas between M_{ov}^{inf} and M_{ov}^{sup}, the free parameter λ_{OV} increases linearly from 0 to 0.2. An example of how we fix the values of M_{ov}^{inf} and M_{ov}^{sup} is shown in Figure 1: for the selected metallicity, M_{ov}^{inf} is equal to $1.08\,M_\odot$, while M_{ov}^{sup} is equal to $1.42\,M_\odot$.

This criterion is obviously somehow arbitrary. It is based on numerical experiments we performed comparing the model predictions with empirical benchmarks such as eclipsing binaries and intermediate-age star clusters, as shown in Section 6. Our choice indirectly introduces a dependence of M_{ov}^{inf} and M_{ov}^{sup} on the initial metallicity (see Table 2). This is because the relationship between M_{cc}^{min} and the total mass of the model depends on the efficiency of H burning via the CNO cycle, which in turn is affected by a change of the absolute value of the total CNO abundance.

The values of M_{ov}^{inf} and M_{ov}^{sup} for each initial chemical composition of our model grid are listed in Table 2. This

Table 2
Grid of Initial Chemical Abundances and Corresponding Values (in Solar Masses) of M_{ov}^{inf} and M_{ov}^{sup} (See the Text for Details)

Z	Y	[Fe/H]	M_{ov}^{inf}	M_{ov}^{sup}
0.00001	0.2470	−3.20	1.30	2.09
0.00005	0.2471	−2.50	1.30	1.78
0.00010	0.2471	−2.20	1.30	1.68
0.00020	0.2472	−1.90	1.30	1.59
0.00031	0.2474	−1.70	1.30	1.54
0.00044	0.2476	−1.55	1.30	1.50
0.00062	0.2478	−1.40	1.32	1.47
0.00079	0.2480	−1.30	1.32	1.45
0.00099	0.2483	−1.20	1.24	1.44
0.00140	0.2488	−1.05	1.21	1.43
0.00197	0.2496	−0.90	1.17	1.42
0.00311	0.2511	−0.70	1.13	1.42
0.00390	0.2521	−0.60	1.10	1.42
0.00614	0.2550	−0.40	1.09	1.42
0.00770	0.2571	−0.30	1.08	1.42
0.00964	0.2596	−0.20	1.08	1.42
0.01258	0.2635	−0.08	1.08	1.43
0.01721	0.2695	0.06	1.09	1.43
0.02081	0.2742	0.15	1.11	1.47
0.02865	0.2844	0.30	1.10	1.42
0.03905	0.2980	0.45	1.09	1.40

approach is different from the previous BaSTI release where, regardless of the chemical composition, we fixed the overshoot efficiency to its maximum value ($\lambda_{OV} = 0.2$) for initial masses larger than or equal to 1.7 $M_{\odot}$, decreasing linearly down to zero when the initial mass is equal to 1.1 $M_{\odot}$.

Before closing this discussion, it is interesting to compare our recipe for decreasing λ_{OV} with decreasing initial mass, with the results of a recent calibration by Claret & Torres (2016). These authors compared their own model grid with the effective temperatures and radii of a sample of detached double-lined eclipsing binaries with well-determined masses, in the [Fe/H] range between about solar and ~ -1.01. They determined λ_{OV} equal to zero for masses lower than about 1.2 $M_{\odot}$, increasing to 0.2 in the mass range between 1.2 $M_{\odot}$ and 2 $M_{\odot}$. For masses larger than 2 $M_{\odot}$, λ_{OV} is equal to ∼0.2, as in our calculations. In the same metallicity range, the value we adopt for M_{ov}^{inf} ranges between ∼1.1 $M_{\odot}$ and ∼1.2 $M_{\odot}$, whereas M_{ov}^{sup} is always equal to ∼1.4 $M_{\odot}$, about 0.6 $M_{\odot}$ smaller than the Claret & Torres (2016) result. It is, however, very difficult to compare the two sets of results. Apart from possible intrinsic differences in the models, Claret & Torres (2016) also determine from their fits the individual values of the mixing length for each component and the initial metallicity Z of each system, and allowed age differences of up to 5% between the components of each system. They derived often systematically lower metallicities than the corresponding spectroscopic measurements. In Section 6, we will see that our models fit well the mass–radius relationship of the systems KIC 8410637 and OGLE-LMC-ECL-15260 (this latter also studied by Claret & Torres 2016), whose masses are in the 1.3 $M_{\odot}$–1.5 $M_{\odot}$ range, bracketing the upper limit where λ_{OV} reached 0.2 with our calibration. We have imposed in our comparisons equal ages for both systems and no variation of the mixing length, and used models with chemical composition consistent with the spectroscopic measurements.

In case of core He burning of low- and intermediate-mass stars, we model core mixing with the semiconvective formalism by Castellani et al. (1985) and breathing pulses inhibited following Caputo et al. (1989). During core He burning in massive stars, we use the Schwarzschild criterion without overshooting to fix the boundary of the mixed region.

We do not include overshooting from the lower boundaries of convective envelopes.

2.3. Radiative and Electron Conduction Opacities

The sources for the radiative Rosseland opacity are the same as for the previous BaSTI calculations. In more detail, opacities are from the OPAL calculations (Iglesias & Rogers 1996) for temperatures larger than $\log(T) = 4.0$, whereas calculations by Ferguson et al. (2005)—including contributions from molecules and grains—have been adopted for lower temperatures. Both high- and low-temperature opacity tables have been computed for the solar-scaled heavy element distribution listed in Table 1.

As for the electron conduction opacities, which are at variance with the models presented in Pietrinferni et al. (2004, 2006), we have now adopted the results by Cassisi et al. (2007). As shown by Cassisi et al. (2007), these opacity calculations affect only slightly (small decrease) the He-core mass at He ignition for low-mass models, and the luminosity of the following horizontal branch (HB) phase (small decrease), compared to the BaSTI calculations that were based on the Potekhin (1999) conductive opacities. For more details on this issue, we refer the reader to the quoted reference as well as to Serenelli et al. (2017).

2.4. Equation of State

As in Pietrinferni et al. (2004), we use the detailed EOS by A. Irwin.[10] A brief discussion of the characteristics of this EOS can be found in Cassisi et al. (2003). We recomputed all required EOS tables for the heavy element distribution in Table 1, adopting the option "*EOS1*" in Irwin's code. This option—recommended by A. Irwin (see also the discussion in Cassisi et al. 2003)—provides the best match to the OPAL EOS (Rogers & Nayfonov 2002) and to the Saumon et al. (1995) EOS in the low-temperature and high-density regime.

2.5. Nuclear Reaction Rates

The nuclear reaction rates are from the NACRE compilation (Angulo et al. 1999), with the exception of the three following reactions, whose rates come from recent re-evaluations:

1. ^{3}He(^{4}He, γ)^{7}Be—Cyburt & Davids (2008),
2. ^{14}N(p, γ)^{15}O—Formicola et al. (2004), and
3. ^{12}C(α, γ)^{16}O—Hammer et al. (2005).

The previous BaSTI calculations employed the NACRE rates (Angulo et al. 1999) for all reactions with the exceptions of the ^{12}C(α, γ)^{16}O rate taken from Kunz et al. (2002)

The first two reaction rates are important for H burning; indeed, the ^{14}N(p, γ)^{15}O reaction is crucial among those involved in the CNO cycle, because it is the slowest one. The impact of this recent ^{14}N(p, γ)^{15}O rate on stellar evolution models has been investigated by Imbriani et al. (2004), Weiss et al. (2005), and Pietrinferni et al. (2010). However, we have repeated the analysis here to verify the expected variation with

[10] The EOS code is made publicly available at http://freeeos.sourceforge.net/ under the GNU General Public License.

respect to the previous BaSTI calculations, due to the combined effects of using the new rates for both ^{3}He(^{4}He, γ)^{7}Be and ^{14}N(p, γ)^{15}O nuclear reactions. When all other physics inputs are kept fixed, we have found that:

1. for a 0.8 $M_\odot$, $Z = 0.0003$ model, the luminosity at the MS turnoff (TO) increases by $\Delta \log(L/L_\odot) \sim 0.02$, while the age increases by about 210 Myr when passing from the NACRE reaction rates used in the previous BaSTI calculations to the ones adopted for the new models. For the same mass but with a metallicity $Z = 0.008$, the effects are smaller, with the MS TO luminosity increased by about 0.01 dex and the age increased by ∼30 Myr;
2. as for the evolution along the red giant branch (RGB), the effect of the new rates on the RGB bump luminosity is completely negligible at $Z = 0.008$, while the RGB bump luminosity increases by $\Delta \log(L/L_\odot) \sim 0.04$ at $Z = 0.0003$. Regardless of the metallicity, the use of the new rates decreases the RGB tip brightness by $\Delta \log(L/L_\odot) \sim 0.02$, in agreement with the results by Pietrinferni et al. (2010) and Serenelli et al. (2017).

The ^{12}C(α, γ)^{16}O reaction is one of the most critical nuclear processes in stellar astrophysics because of its impact on a number of astrophysical problems (see, e.g., Cassisi et al. 2003; Cassisi & Salaris 2013, and references therein). The more recent assessment of this reaction rate is not significantly different from Kunz et al. (2002) as used by Pietrinferni et al. (2004). As a consequence, the use of this new rate has a small impact on the models: for instance, the core He-burning lifetime is decreased by a negligible ∼0.2% when using this new rate compared to models calculated with the older Kunz et al. (2002) rate.

As in the previous BaSTI calculations, electron screening is calculated according to the appropriate choice among strong, intermediate, and weak, following Dewitt et al. (1973) and Graboske et al. (1973).

2.6. Neutrino Energy Losses

Neutrino energy losses are included with the same prescriptions as in the previous BaSTI calculations. For plasma neutrinos, we use the rates by Haft et al. (1994), supplemented by the Munakata et al. (1985) rates for the other relevant neutrino production processes.

2.7. Superadiabatic Convection and Outer Boundary Conditions

The combined effect of the treatment of the superadiabatic layers of convective envelopes and the method to determine the outer boundary conditions of the models has a major impact on the effective temperature scale of stellar models with deep convective (or fully convective) envelopes.

As in the previous BaSTI models, we treat the superadiabatic convective layers according to the Böhm-Vitense (1958) flavor of the mixing-length theory, using the formalism by Cox & Giuli (1968). The value of the mixing-length parameter $\alpha_{\rm ML}$ is fixed by the solar model calibration to 2.006 (see Section 3 for more details) and kept the same for all masses, initial chemical compositions, and evolutionary phases.

In the previous BaSTI models, the outer boundary conditions were obtained by integrating the atmospheric layers employing the $T(\tau)$ relation provided by Krishna Swamy (1966). In this new release, we decided to employ the alternative solar semi-empirical $T(\tau)$ by Vernazza et al. (1981). More specifically, we implemented in our evolutionary code the following fit to the tabulation provided by Vernazza et al. (1981):

$$T^4 = 0.75\ T_{\rm eff}^4\ (\tau + 1.017 - 0.3e^{-2.54\tau} - 0.291e^{-30\tau}). \quad (1)$$

As shown by Salaris & Cassisi (2015), model tracks computed with this $T(\tau)$ relation approximate well the results obtained using the hydro-calibrated $T(\tau)$ relationships determined from the 3D radiation hydrodynamics calculations by Trampedach et al. (2014) for the solar chemical composition. Figure 2 shows the Hertzsprung–Russell diagram (HRD) of 0.85 $M_\odot$ evolutionary tracks from the pre-MS to the tip of the RGB, computed for the three labelled initial metallicities. The physics inputs are kept the same as in the old BaSTI calculations, but for the $T(\tau)$ relation, they are either from Krishna Swamy (1966) or Vernazza et al. (1981). For both choices, the value of $\alpha_{\rm ML}$ has been fixed by an appropriate solar calibration.

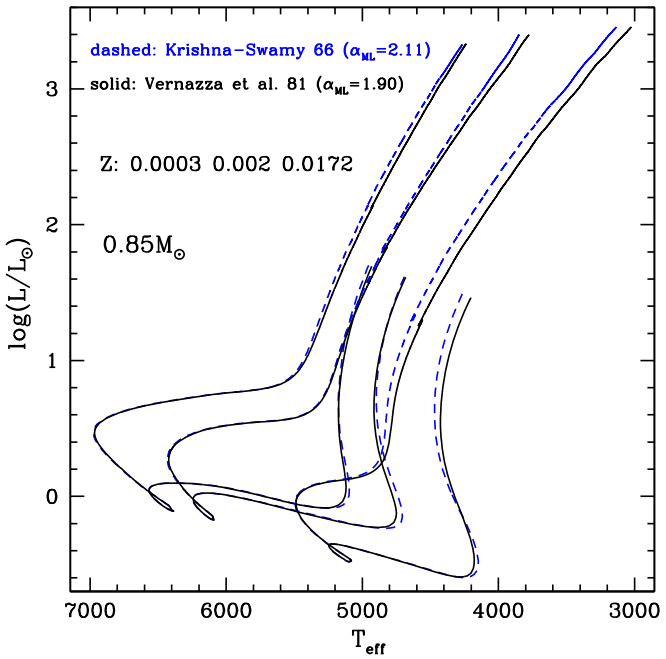

Figure 2. Hertzsprung–Russell diagrams of models computed with two different assumptions about the $T(\tau)$ relation used to calculate the outer boundary conditions for the labelled mass and metallicities. The solar-calibrated mixing-length values for each choice of the $T(\tau)$ relation are also shown.

The two sets of models overlap almost perfectly along the MS at all Z, whereas some differences in $T_{\rm eff}$ at fixed luminosity appear along the RGB (and the pre-MS). Differences are of about 60 K at the lowest metallicity, reaching ∼90 K at solar metallicity. Tracks calculated with the Vernazza et al. (1981) $T(\tau)$ are always the cooler ones. For a more detailed discussion on the impact of different $T(\tau)$ relations on the $T_{\rm eff}$ scale of RGB stellar models, we refer to Salaris & Cassisi (2015) and references therein.

In the first release of BaSTI, the minimum stellar mass was set to 0.50 $M_\odot$ for all chemical compositions, while these new calculations include the mass range below 0.50 $M_\odot$, down to 0.10 $M_\odot$. As extensively discussed in the literature (see, e.g., Baraffe et al. 1995; Allard et al. 1997; Brocato et al. 1998; Chabrier & Baraffe 2000, and references therein), in this

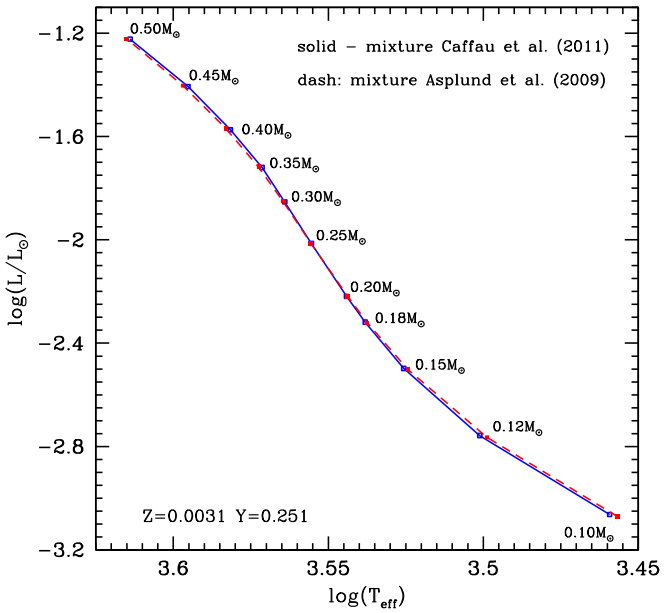

Figure 3. Hertzsprung–Russell diagram of core H-burning models for an age of 10 Gyr and the labelled initial chemical composition and masses. Boundary conditions have been obtained from model atmospheres calculated using the labelled solar heavy element mixtures (see the text for details).

regime of so-called very low-mass (VLM) stars, i.e., $M \leqslant 0.45\,M_{\odot}$, outer boundary conditions provided by accurate non-gray model atmospheres are required. Therefore, for the VLM model calculations, we employed boundary conditions (pressure and temperature at a Rosseland optical depth $\tau = 100$) taken from the PHOENIX model atmosphere library[11] (Allard et al. 2012 and references therein), more precisely the BT-Settl model set. These model atmospheres properly cover the required parameter space in terms of effective temperature, surface gravity, and metallicity range. However, this set of models has been computed for the Asplund et al. (2009) solar heavy element distribution, which is different from the one adopted in our calculations (see Section 2.1).

One could argue that this difference in the heavy element mixture may have an impact on the predicted spectral energy distribution, but it should have only a minor effect on the model atmosphere structure, hence on the derived outer boundary conditions. We have verified this latter point as follows. The PHOENIX model atmosphere repository contains a subset of models—labelled CIFIST2011—computed with the same solar heavy element distribution as in our calculations (Caffau et al. 2011), for a few selected metallicities. We have calculated sets of VLM models using, alternatively, the PHOENIX boundary conditions for the Asplund et al. (2009) mixture and the Caffau et al. (2011) one. Figure 3 shows the result of such a comparison for one selected metallicity. As expected, the two sets of VLM calculations provide very similar HRDs. Differences in bolometric luminosity and effective temperature are vanishingly small for masses larger than $\sim 0.12\,M_{\odot}$, while they are equal to just $\Delta \log(L/L_{\odot}) \sim 0.007$ and $\Delta T_{\rm eff} \sim 16$ K for smaller masses.

We close this section with more details on the transition from VLM models with outer boundary conditions determined from PHOENIX model atmospheres to models calculated with the $T(\tau)$ relation in Equation (1). To achieve a smooth transition in the $\log(L/L_{\odot})$—$T_{\rm eff}$ diagram between the two regimes, for each chemical composition, we computed models with mass up to $0.70\,M_{\odot}$ with the PHOENIX boundary conditions, and models with mass down to $0.4\,M_{\odot}$ using the $T(\tau)$ relation. In the overlapping mass range, we selected a specific transition mass corresponding to the pair of models—which happens to fall in the range between $\sim 0.5 M_{\odot}$ and $\sim 0.65 M_{\odot}$, depending on the initial composition—showing negligible differences in both bolometric luminosity and effective temperature, typically $\Delta T_{\rm eff} \leqslant 25$ K and $\Delta \log(L/L_{\odot}) \leqslant 0.004$. For masses equal to and lower than this mass, we keep the calculations with PHOENIX boundary conditions, and above this limit the models with $T(\tau)$ integration. This allows the isochrones displaying a smooth transition between the two boundary condition regimes to be calculated.

2.8. Mass Loss

Mass loss is included in the Reimers (1975) formula, as in the previous BaSTI models. The free parameter η entering this mass-loss prescription has been set equal to 0.3, following the *Kepler* observational constraints discussed in Miglio et al. (2012). We also provide stellar models computed without mass loss ($\eta = 0$). The previous BaSTI calculations included three options, $\eta = 0$, 0.2, and 0.4.[12]

3. The Standard Solar Model

As already mentioned, the calibration of the SSM sets the value of $\alpha_{\rm ML}$ and the initial solar He abundance and metallicity. At the solar age ($t_{\odot} = 4.57$ Gyr; Bahcall et al. 1995), our $1\,M_{\odot}$ SSM (including the diffusion of both He and metals and calculated starting from the pre-MS) matches the luminosity, radius ($L_{\odot} = 3.842 \times 10^{33}$ erg s^{-1} and $R_{\odot} = 6.9599 \times 10^{10}$ cm, respectively, as given by Bahcall et al. 1995), and the present $(Z/X)_{\odot}$ Caffau et al. (2011) abundance ratio with initial abundances $Z_{\odot}^{\rm ini} = 0.01721$ and $Y_{\odot}^{\rm ini} = 0.2695$, and mixing length $\alpha_{\rm ML} = 2.006$.

Our SSM has a surface He abundance $Y_{\odot,\rm surf} = 0.238$ and a radius of the boundary of the surface convective zone $R_{\rm CZ}/R_{\odot}$ equal to 0.722. These values have to be compared with the asteroseismic estimates $R_{\rm CZ}/R_{\odot} = 0.713 \pm 0.001$ (Basu 1997) and $Y_{\odot,\rm surf} = 0.2485 \pm 0.0035$ (Basu & Antia 2004). These differences between models and observations are common to all SSMs based on the revised solar surface compositions discussed before (e.g., Basu & Antia 2004; Vinyoles et al. 2017, and references therein). Differences are larger when using the lower Z solar abundances of Asplund et al. (2009), as discussed by Choi et al. (2016). This is an open problem, and efforts are being devoted to explore the possibility of suitable changes to the SSM input physics, such as radiative opacities (we refer to Villante 2010; Krief et al. 2016; Vinyoles et al. 2017, for a detailed analysis of this issue).

4. The Stellar Model Library

Our new model library increases significantly the number of available metallicities, compared to the old BaSTI calculations. We have calculated models for 22 metallicities ranging from $Z = 10^{-5}$

[11] The model atmosphere data set is publicly available at the following URL: http://phoenix.ens-lyon.fr/Grids/.

[12] The release of the previous BaSTI models with $\eta = 0$ is not directly available at the old URL site, but can be obtained by request.

Table 3
Various Grids of Stellar Models Provided in the Database

Case	Convective Overshooting	Mass-loss Efficiency	Diffusion
a	Yes	$\eta = 0.3$	Yes
b	Yes	$\eta = 0.3$	No
c	Yes	$\eta = 0.0$	No
d	No	$\eta = 0.0$	No

up to ∼0.04; the exact values are listed in Table 2. We adopted a primordial He abundance $Y = 0.247$ based on the cosmological baryon density following *Planck* results (Coc et al. 2014). With this choice of primordial He abundance and the initial solar He abundance obtained from the SSM calibration, we obtain a He-enrichment ratio $dY/dZ = 1.31$, which we have used in our model grid computation. For each metallicity, the corresponding initial He abundance and [Fe/H] are listed in Table 2.

4.1. Evolutionary Tracks

As with the first release of the BaSTI database, we have calculated several model grids by varying one at a time some modeling assumptions. A schematic overview of all grids made available in the new BaSTI repository is provided in Table 3. Our reference set of models is set (a) in Table 3, which includes MS convective core overshooting, mass loss with $\eta = 0.3$, and atomic diffusion of He and metals.

For each chemical composition (and choice of modeling assumptions), we have computed 56 evolutionary sequences. The minimum initial mass is $0.1\,M_{\odot}$, while the maximum value is $15\,M_{\odot}$). For initial masses below $0.2\,M_{\odot}$, we computed evolutionary tracks for masses equal to 0.10, 0.12, 0.15, and $0.18\,M_{\odot}$. In the range between 0.2 and $0.7\,M_{\odot}$ a mass step equal to $0.05\,M_{\odot}$ has been adopted. Mass steps equal to $0.1\,M_{\odot}$, $0.2\,M_{\odot}$, $0.5\,M_{\odot}$, and $1\,M_{\odot}$ have been adopted for the mass ranges 0.7–2.6 $M_{\odot}$, 2.6–3.0 $M_{\odot}$, and 3.0–10.0 $M_{\odot}$, and masses larger than $10.0\,M_{\odot}$, respectively.

Models less massive than $4.0\,M_{\odot}$ have been computed from the pre-MS, whereas more massive models have been computed starting from a chemically homogeneous configuration on the MS. Relevant to pre-MS calculations, the adopted mass fractions for D, ^{3}He, and ^{7}Li are equal to 3.9×10^{-5}, 2.3×10^{-5}, and 2.6×10^{-9}, respectively.

All stellar models—except for the less massive ones whose core H-burning lifetime is longer than the Hubble time—have been calculated until the start of the thermal pulses (TPs)[13] on the AGB, or C-ignition for the more massive ones. For the long-lived low-mass models, we stopped the calculations when the central H mass fraction is ∼0.3 (corresponding to ages already much older than the Hubble time).

For each initial chemical composition, we also provide an extended set of core He-burning models suitable for the study of the HB in old stellar populations. We have considered different values of the total mass (with fine mass spacing, as in Pietrinferni et al. 2004) but the same mass for the He core and the same envelope chemical stratification, corresponding to an RGB progenitor at the He flash for an age of ∼12.5 Gyr.

All evolutionary tracks presented in this work have been reduced to the same number of points ("normalized") to calculate isochrones (see, e.g., Dotter 2016 for a discussion of this issue) and for ease of interpolation, by adopting the same approach extensively discussed in Pietrinferni et al. (2004) and updated in Pietrinferni et al. (2006). This method is based on the identification of some characteristic homologous points (key points) corresponding to well-defined evolutionary stages along each individual track (see Pietrinferni et al. 2004 for more details on this issues). Given that almost all evolutionary tracks now include the pre-MS stage, we added three additional key points compared to the previous BaSTI calculations. The first one is taken at an age of 10^{4} yr, the second one corresponds to the end of the deuterium-burning stage, while the third key point is set at the first minimum of the surface luminosity for all models but the VLM ones. For these latter masses, this point corresponds to the stage when the energy produced by the p–p chain starts to dominate the energy budget. The fourth key point corresponds to the zero-age MS (ZAMS), defined as the model fully sustained by nuclear reactions, with all secondary elements at their equilibrium abundances.[14] However, for VLM models that attain nuclear equilibrium of the secondary elements involved in the p–p chain over extremely long timescales, this key point corresponds to the first minimum of the bolometric luminosity. All subsequent key points are fixed exactly as in the previous BaSTI database. Table 4 lists the correspondence between key points and evolutionary stages as well as the corresponding line number in the normalized evolutionary track, while Figure 4 shows the location of a subset of key points (the first 10) on selected evolutionary tracks.

Table 4
Correspondence between Evolutionary Stage, Key Point, and Line Number of the Normalized Tracks

Key Point	Line	Evolutionary Phase
1	1	Age equal to 1000 years
2	20	End of deuterium burning
3	60	The first minimum in the surface luminosity, or when nuclear energy starts to dominate the energy budget
4	100	Zero-age main sequence or minimum in bolometric luminosity for VLM models
5	300	First minimum of $T_{\rm eff}$ for high-mass or central H mass fraction X_c=0.30 for low-mass and VLM models
6	360	Maximum in $T_{\rm eff}$ along the MS (TO point)
7	420	Maximum in $\log(L/L_{\odot})$ for high-mass or X_c=0.0 for low-mass models
8	490	Minimum in $\log(L/L_{\odot})$ for high-mass or base of the RGB for low-mass models
9	860	Maximum luminosity along the RGB bump
10	890	Minimum luminosity along the RGB bump
11	1290	Tip of the RGB
12	1300	Start of quiescent core He burning
13	1450	Central abundance of He equal to 0.55
14	1550	Central abundance of He equal to 0.50
15	1650	Central abundance of He equal to 0.40
16	1730	Central abundance of He equal to 0.20
17	1810	Central abundance of He equal to 0.30
18	1950	Central abundance of He equal to 0.00
19	2100	Energy associated with the CNO cycle becomes larger than that provided by He burning

[13] In the near future, we plan to extend these computations to the end of the TP phase using the synthetic AGB technique (see, e.g., Cordier et al. 2007 and references therein).

[14] This stage also corresponds to the minimum luminosity during the core H-burning stage.

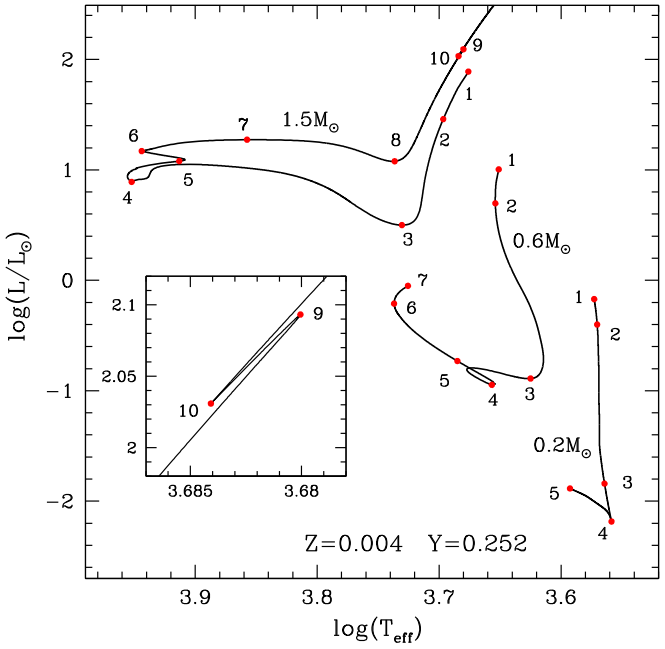

Figure 4. Hertzsprung–Russell diagram of selected evolutionary tracks and the labelled initial chemical composition. We also show the position of the first 10 key points used to normalize the tracks. The inset is an enlargement of the RGB bump phase to show the exact position of key points 9 and 10.

For each chemical composition, these normalized evolutionary tracks are used to compute extended sets of isochrones for ages between 20 Myr and 14.5 Gyr (older isochrones can also be computed on request).

Figure 5 shows an example of the full set of reference tracks and isochrones calculated for one chemical composition ($Y = 0.2695$, $Z = 0.01721$). Panel (a) displays the full grid of tracks for masses ranging from 0.1 $M_\odot$ to 15 $M_\odot$, while panel (c) focuses on the RGB region for a subset of models with mass between 0.4 $M_\odot$ and 4.5 $M_\odot$ (dotted lines denote the pre-MS evolution of the same models). The set of HB tracks is shown in panel (d) for an RGB progenitor mass equal to 1.0$M_\odot$ and minimum HB mass equal to 0.4727 $M_\odot$, while panel (e) displays a subset of pre-MS, MS, and RGB tracks with mass between 0.1$M_\odot$ and 1.0$M_\odot$. Finally, panel (b) displays a set of isochrones with ages equal to 20 Myr, 100 Myr, 500 Myr, 1 Gyr, 4 Gyr, and 14 Gyr, respectively (solid lines), overlaid onto the full set of tracks (dashed lines).

4.2. Bolometric Corrections

Bolometric luminosities and effective temperatures along evolutionary tracks and isochrones need to be translated to magnitudes and colors in sets of photometric filters for comparison with observed color–magnitude diagrams (CMDs) and to predict integrated fluxes of unresolved stellar populations. This requires sets of stellar spectra covering the relevant parameter space in terms of metallicity, surface gravity, and effective temperature of the models. To such aim, a new grid of model atmospheres has been computed using the latest version of the ATLAS9 code[15] originally developed by Kurucz (1970). ATLAS9 allows one-dimensional, plane-parallel model atmospheres to be calculated under the assumption of local thermodynamical equilibrium for all species. The method of the opacity distribution function (ODF; Kurucz et al. 1974) is employed to handle the line opacity by pretabulating the line opacity as a function of gas pressure and temperature in a given number of wavelength bins. ODFs and Rosseland mean opacity tables are calculated for a given metallicity (fixing the chemical mixture) and for a given value of microturbulent velocity. Even if the computation of ODFs can be time consuming, the calculation of any model atmosphere (defined by its effective temperature and gravity) for the metallicity and microturbulent velocity corresponding to the adopted ODF turns out to be very fast.

Table 5
Effective Temperature and Surface Gravity Ranges Covered by Our New Grid of ATLAS9 Model Atmospheres and Spectra, Together with the Grid Spacings $\Delta_{T_{\rm eff}}$ and $\Delta_{\log(g)}$

$T_{\rm eff}$ (K)	$\Delta_{T_{\rm eff}}$ (K)	$\log(g)$ (cgs)	$\Delta_{\log(g)}$ (cgs)
3500–6000	250	0.0–5.0	0.5
6250–7500	250	0.5–5.0	0.5
7750–8250	250	1.0–5.0	0.5
8500–9000	250	1.5–5.0	0.5
9250–11,750	250	2.0–5.0	0.5
12,000–13,000	250	2.5–5.0	0.5
13,000–19,000	1000	2.5–5.0	0.5
20,000–26,000	1000	3.0–5.0	0.5
27,000–31,000	1000	3.5–5.0	0.5
32,000–39,000	1000	4.0–5.0	0.5
40,000–49,000	1000	4.5–5.0	0.5
50,000	…	5.0	…

Grids of ATLAS9 model atmospheres based on suitable ODFs are freely available but based on different solar chemical abundances compared to the one used in our calculations. The grid by Castelli & Kurucz (2004) adopted the solar abundances by Grevesse & Sauval (1998), which were computed by Kirby (2011) using the abundances of Anders & Grevesse (1989), while the recent one by Mészáros et al. (2012) for the APOGEE survey used the abundances by Asplund et al. (2005). For the new grid presented here, we adopted the same solar metal distribution of the stellar evolution calculations. For the computation of the new ODFs, Rosseland opacity tables, and model atmospheres, we followed the scheme described in Mészáros et al. (2012).

For each [Fe/H] and microturbulent velocity, one ODF and one Rosseland opacity table are calculated using the codes DFSYNTHE and KAPPA9 (Castelli 2005), respectively. The [Fe/H] grid ranges from −4.0 to +0.5 dex in steps of 0.5 dex from −4.0 to −3.0 dex, and in steps of 0.25 dex for the other metallicities, assuming solar-scaled abundances for all elements. The adopted values for the microturbulent velocities are 0, 1, 2, 4, and 8 km s^{-1}. In the calculation of the ODFs, we included all atomic and molecular transitions listed in F. Castelli's web site[16]; in particular, the line list for TiO is from Schwenke (1998) and that for H_2O is from Langhoff et al. (1997).

For each [Fe/H] (but adopting only the microturbulent velocity of 2 km s^{-1}) a grid of ATLAS9 model atmospheres has been computed, covering the effective temperature–surface gravity parameter space summarized in Table 5, for a total of 475 models.

Similarly to those computed by Castelli & Kurucz (2004), these new model atmospheres include 72 plane-parallel layers ranging from $\log\tau = -6.875$ (where τ is the Rosseland optical

[15] http://wwwuser.oats.inaf.it/castelli/sources/atlas9codes.html

[16] http://wwwuser.oats.inaf.it/castelli/linelists.html

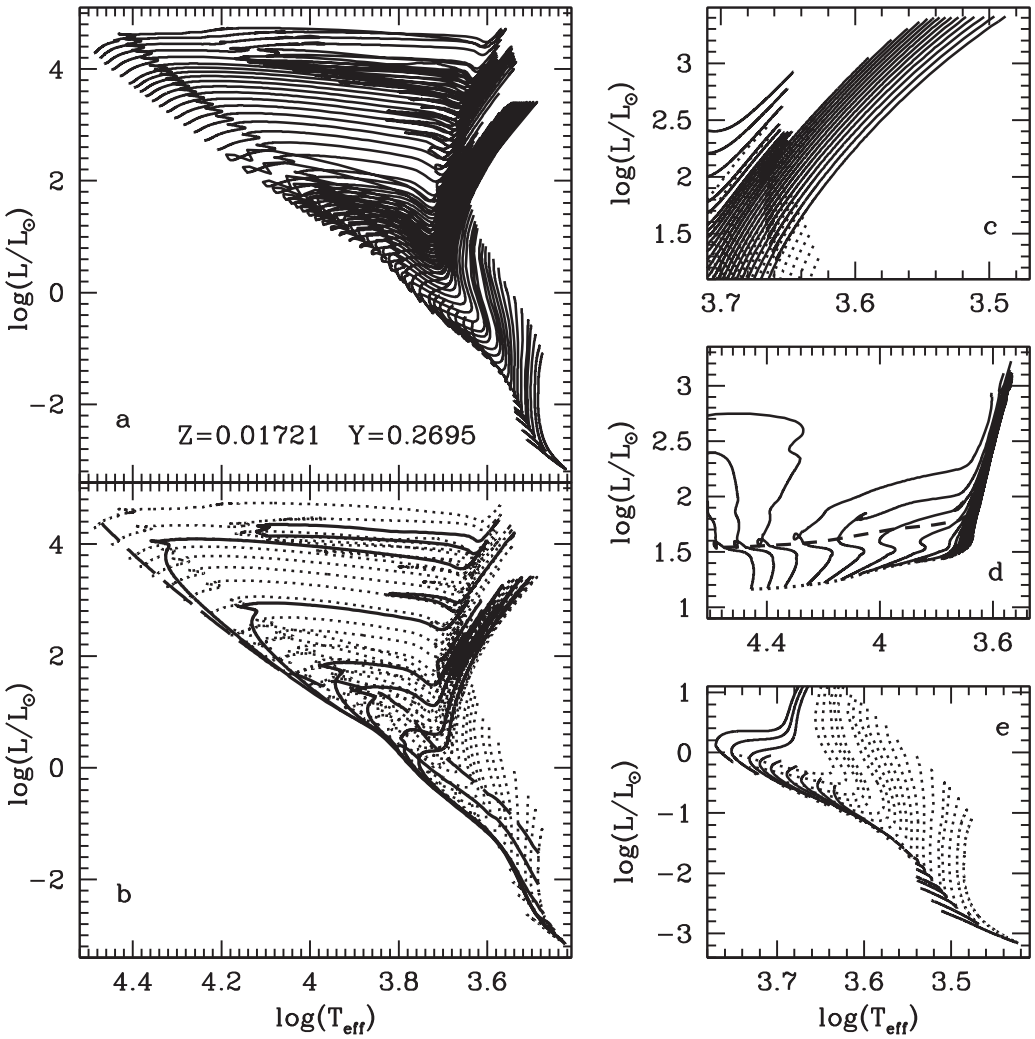

Figure 5. Hertzsprung–Russell diagrams of the full set of reference tracks and isochrones calculated for the labelled initial chemical composition (panel a), and a subset of isochrones for 5 Myr (long dashed line), and 20 Myr, 100 Myr, 500 Myr, 1 Gyr, 4 Gyr, and 14 Gyr, solid lines in panel (b), overlaid onto the track grid (dashed lines). Panel (c) shows selected RGB tracks (solid lines) and part of their pre-MS evolution (dotted lines), while panel (d) displays the full set of HB tracks. The zero-age HB is shown as a dotted line, while the dashed line corresponds to the central He exhaustion. Panel (e) displays a subset of pre-MS (dotted), MS, and RGB tracks with mass between $0.1M_{\odot}$ and $1.0M_{\odot}$ (see the text for details).

depth) to +2.00, in steps of 0.125, and have been computed with the overshooting option switched off, adopting a mixing-length equal to 1.25 as in previous calculations. For each model atmosphere, the corresponding emerging flux has then been computed.

The ATLAS9 grid of spectra is complemented by two additional spectral libraries to cover the parameter space of cool giants and low-mass dwarfs. At low $T_{\rm eff}$ and surface gravities, we use the BaSeL WLBC99 results (Westera et al. 1999, 2002). This is a semi-empirical library, built from a grid of theoretical spectra that have been later calibrated to match empirical color–$T_{\rm eff}$ relations from neighborhood stars. These templates are available in the metallicity range $-2.0 \leqslant$ [Fe/H] $\leqslant 0.5$, in steps of 0.5 dex. For the low $T_{\rm eff}$ and high gravity regime, we use spectra from the Göttingen Spectral Library (Husser et al. 2013). These have been calculated using the code PHOENIX (Hauschildt & Baron 1999), which is particularly suited to model atmospheres of cool dwarfs. The PHOENIX configuration used for this library employs a variable parametrization of microturbulence and mixing length, depending on the properties of the modeled atmosphere. The metallicity coverage is $-4.0 \leqslant$ [Fe/H] $\leqslant 1.0$, in steps of 0.5 dex. Figure 6 shows the range of effective temperature and surface gravity covered by our adopted spectral libraries.

We have computed tables of BCs for several popular photometric systems (the complete list is found in Table 6), following the prescription by Girardi et al. (2002) for photon-counting defined systems:

$$\mathrm{BC}_{S_\lambda} = M_{\mathrm{bol},\odot} - 2.5\log\left[4\pi(10\ \mathrm{pc})^2 F_{\mathrm{bol}}/L_\odot\right] + 2.5\log\left(\frac{\int_{\lambda_1}^{\lambda_2}\lambda F_\lambda S_\lambda d\lambda}{\int_{\lambda_1}^{\lambda_2}\lambda f^0_\lambda S_\lambda d\lambda}\right) - m^0_{S_\lambda}, \quad (2)$$

where S_λ is a generic filter response curve, defined between λ_1 and λ_2, $F_{\rm bol} = \sigma\ T^4_{\rm eff}$ is the total emerging flux at the stellar surface, F_λ is the stellar emerging flux at a given wavelength, f^0_λ is the wavelength-dependent flux of a reference spectrum and $m^0_{S_\lambda}$ is the magnitude of the reference spectrum in the filter S_λ (denoted as zero, point). We adopt $M_{\mathrm{bol},\odot} = 4.74$, following the IAU B2 resolution of 2015 (Mamajek et al. 2015).

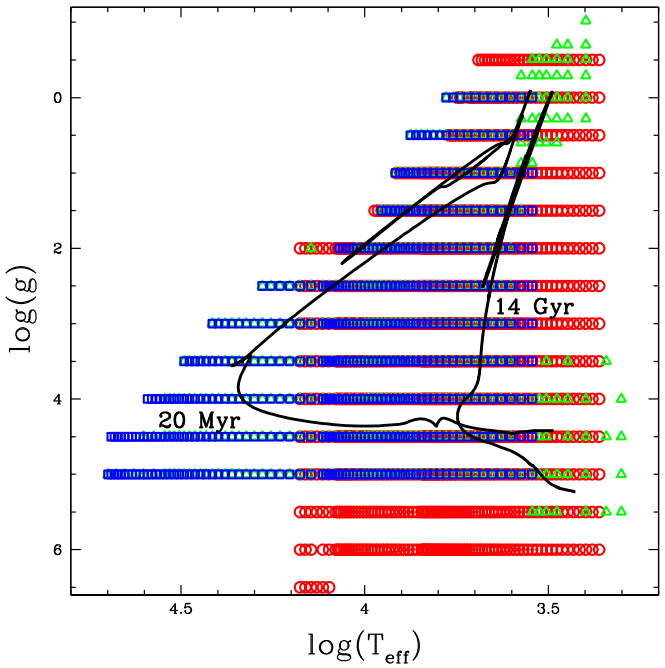

Figure 6. $T_{\rm eff}$–log(g) coverage ([Fe/H] = 0) of the adopted spectral libraries. Different symbols correspond to our ATLAS9 grid (blue diamonds), and the WLBC99 (green triangles), and the Göttingen (red circles) spectral libraries. Two solar metallicity isochrones for 20 Myr and 14 Gyr are also shown.

The reference spectra are either the spectrum of Vega (α Lyr), for systems that use Vega for the magnitude zero-points (Vegamag systems), or a spectrum with constant flux density per unit frequency $f_\nu^0 = 3.631 \cdot 10^{-20}$ erg s^{-1} cm^{-2} Hz^{-1}, for ABmag systems. For older photometric systems, such as the Johnson–Cousins–Glass *UBVRIJHKLM*, we use the energy-integration equivalent of Equation (2).

Due to the differences between the adopted sets of spectral libraries, the resulting BCs display non-negligible differences in the overlapping $T_{\rm eff}$ and surface gravity regimes. To eliminate discontinuities in the final merged BC set, the different sets were matched smoothly in the overlapping regions by applying some suitable ramping at the edges of the various tables. After several tests, we adopted the following combination of BC libraries:

1. at metallicities equal to or lower than solar, we employ the BCs from our ATLAS9 grid, supplemented at gravities lower than log(g) = 0.0 and $T_{\rm eff} < 3700$ K by WLBC99 results; at $T_{\rm eff}$ lower than about 3700 K and log(g) $\geqslant$ 4.5 we switch from our ATLAS9 BCs to Husser et al. (2013) BCs;
2. at supersolar metallicities, we adopt our ATLAS9 BCs for the V band (or equivalent) as well as for bluer photometric passbands, extrapolating linearly in log(g) and $T_{\rm eff}$ when necessary. For redder photometric passbands we use ATLAS9 BCs for gravities lower than log(g) = 0.0 (extrapolated when necessary) and Husser et al. (2013) BCs for gravities larger or equal than log(g) = 4.5, and $T_{\rm eff}$ lower than about 3700 K.

Figure 7 shows examples of our adopted composite BC library.

4.3. Asteroseismic Properties of the Models

Asteroseismology has experienced a revolution thanks to past and present space missions such as *CoRoT* (Baglin et al. 2009), *Kepler* (Gilliland et al. 2010), and K2 (Chaplin et al. 2015), which have provided high-precision photometric data for hundreds of main-sequence and subgiant stars and for thousands of red giants.

Future satellites like *TESS* (Ricker et al. 2014) and *PLATO* (Rauer et al. 2014) hold promise to expand the current sample greatly and thus further extend the impact of asteroseismology in the fields of stellar physics (e.g., Beck et al. 2011; Verma et al. 2014), exoplanet studies (e.g., Huber et al. 2013; Silva Aguirre et al. 2015, and Galactic archaeology (e.g., Casagrande et al. 2016; Silva Aguirre et al. 2017). Given the availability of high-quality oscillation data, we provide the corresponding theoretical quantities to fully exploit their potential.

We have computed adiabatic oscillation frequencies for all of the models using the Aarhus aDIabatic PuLSation package (ADIPLS; Christensen-Dalsgaard 2008). We provide the radial, dipole, quadrupole, and octupole mode frequencies for the models with central hydrogen mass fraction $>10^{-4}$ but only the radial mode frequencies for more evolved models. The power spectrum of the solar-like oscillators have several global characteristic features that can be used to constrain the stellar properties. Some of these features do not require very high signal-to-noise data for their determinations—in contrast to the individual oscillation frequencies that need long time-series data with high signal-to-noise ratio for their measurements—and play a crucial role in ensemble studies. We also provide three such global asteroseismic quantities for the models, viz., the frequency of maximum power ($\nu_{\rm max}$), the large frequency separation for the radial mode frequencies ($\Delta\nu_0$), and the asymptotic period spacing for the dipole mode frequencies (ΔP_1).

The value of $\nu_{\rm max}$ was determined using the well-known scaling relation (Kjeldsen & Bedding 1995)

$$\frac{\nu_{\rm max}}{\nu_{\rm max,\odot}} = \left(\frac{M}{M_\odot}\right)\left(\frac{R}{R_\odot}\right)^{-2}\left(\frac{T_{\rm eff}}{T_{\rm eff,\odot}}\right)^{-1/2}, \quad (3)$$

where M, R, and $T_{\rm eff}$ are the model mass, radius, and effective temperature, respectively. We adopted $\nu_{\rm max,\odot} = 3090\,\mu$Hz from Huber et al. (2011), $T_{\rm eff,\odot} = 5777$ K, and $M_\odot = 1.9891 \times 10^{33}$ gm and $R_\odot = 6.9599 \times 10^{10}$ cm as used in the corresponding stellar tracks. We extracted $\Delta\nu_0$ following White et al. (2011), i.e., by performing a weighted linear least-squares fit to the radial mode frequencies as a function of the radial order, with a Gaussian weighting function centered around $\nu_{\rm max}$, with $0.25\,\nu_{\rm max}$ FWHM. The large frequency separation and frequency of maximum power, together with the measurement of the stellar $T_{\rm eff}$, have been used to determine the masses and radii of large samples of isolated stars, independent of modeling, thus providing strong constraints on stellar evolution models and on models of Galactic stellar populations (see, e.g., Kallinger et al. 2010; Chaplin et al. 2011; Miglio et al. 2012).

We determined the period spacing ΔP_1 using the asymptotic expression

$$\Delta P_1 = \sqrt{2}\,\pi^2\left(\int \frac{N}{r}dr\right)^{-1}, \quad (4)$$

Table 6
Available Photometric Systems

Photometric system	Calibration	Passbands	Zero-points
UBVRIJHKLM	Vegamag	Bessell & Brett (1988); Bessell (1990)	Bessell et al. (1998)
HST–WFPC2	Vegamag	SYNPHOT	SYNPHOT
HST–WFC3	Vegamag	SYNPHOT	SYNPHOT
HST–ACS	Vegamag	SYNPHOT	SYNPHOT
2MASS	Vegamag	Cohen et al. (2003)	Cohen et al. (2003)
DECam	ABmag	DES collaboration	0
Gaia	Vegamag	Jordi et al. (2010)[a]	Jordi et al. (2010)
JWST–NIRCam	Vegamag	*JWST* User Documentation[b]	SYNPHOT
SAGE	ABmag	SAGE collaboration	0
Skymapper	ABmag	Bessell et al. (2011)	0
Sloan	ABmag	Fukugita et al. (1996)	Dotter et al. (2008)
Strömgren	Vegamag	Maíz Apellániz (2006)	Maíz Apellániz (2006)
VISTA	Vegamag	ESO	González-Fernández et al. (2017)

Notes. We also list the source for the passband definitions and reference zero-points.
[a] The nominal *G* passband curve has been corrected following the post-DR1 correction provided by Maíz Apellániz (2017).
[b] https://jwst-docs.stsci.edu/

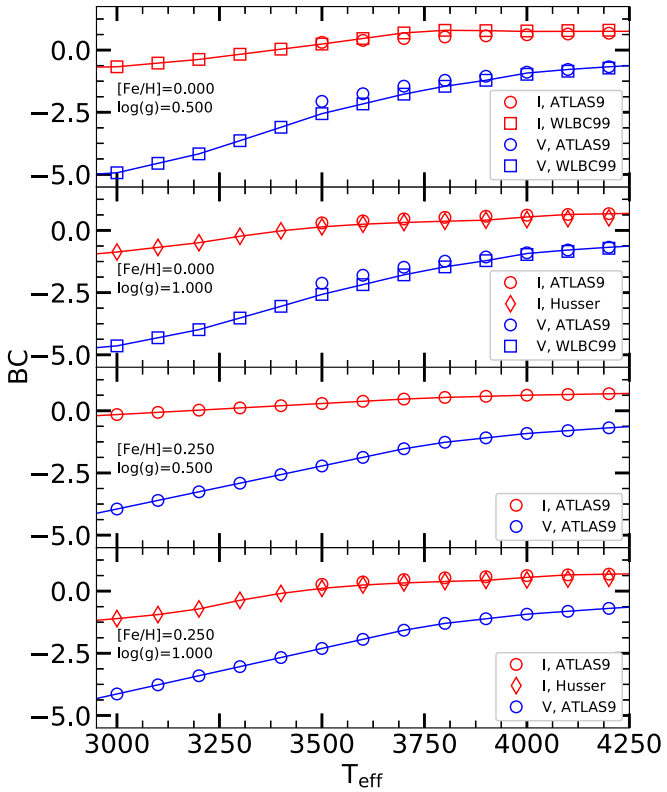

Figure 7. An example of our final BC set (solid lines) for the *V* and *I* photometric passbands, as a function of the effective temperature, for some selected metallicities and surface gravities (see the text for details).

where N and r are the Brunt–Väisälä frequency and radial coordinate, respectively. The integration is performed over the radiative interior. Since N is weighted with r^{-1} in the integral, ΔP_1 is very sensitive to the Brunt–Väisälä frequency profile in the core. Hence, the measurement of ΔP_1 offers a unique opportunity to constrain the uncertain aspects of the physical processes taking place in stellar cores. As an example, Degroote et al. (2010) used the measurement of the period spacing for the star HD 50230 observed using the *CoRoT* satellite to constrain the mixing in its core (see also, Montalbán et al. 2013). Figure 8 illustrates the evolution of models in the $\Delta\nu_0$–ΔP_1 diagram (evolution proceeds from right to left). This is an interesting diagram because $\Delta\nu_0$ contains mostly information about the envelope, whereas ΔP_1 contains mostly information about the core. The hook-like feature on the right (beyond the displayed range for $M = 1.0\ M_\odot$ and $1.5\ M_\odot$) corresponds to the base of the RGB. The sudden jump at the lowest $\Delta\nu_0$ for $M = 1.0\ M_\odot$, $1.5\ M_\odot$, and $2.0\ M_\odot$ is due to the helium flash, which causes the stellar structure to change rapidly in a short period of time. This diagram has been used successfully to distinguish the shell hydrogen-burning red giant stars with those that are fusing helium in the core along with the hydrogen in the shell (e.g., Bedding et al. 2011; Mosser et al. 2011).

5. Comparisons with Existing Model Databases

This section is devoted to comparisons of our isochrones with recent, widely employed isochrone and stellar model databases. The goal is to give a general picture of how our new calculations compare to recent, popular models. The model grids shown in our comparisons are computed by employing various different choices for the input physics and treatment of mixing, and the reference solar metal distribution can also be different (see Tables 7 and 8 for a summary). We show comparisons in the HRD o bypass the additional degree of freedom introduced by the choice of BCs.

We start first with a comparison with our previous BaSTI computations (Pietrinferni et al. 2004), displayed in Figure 9. We show our new isochrones for [Fe/H] = 0.06 and [Fe/H] = −1.55, and ages equal to 30 Myr, 100 Myr, 1 Gyr, 3 Gyr, 5 Gyr, and 12 Gyr, respectively, compared to the older BaSTI release for the same ages, [Fe/H] = 0.06 and [Fe/H] = −1.49 (the metallicity grid point closest to [Fe/H] = −1.55 in the older release) and $\eta = 0.4$. We consider here our new isochrones without diffusion, because the older model grid was calculated by ignoring the atomic diffusion (we are using our set b) of the models as described in Table 3. Core overshooting during the MS is included in both sets of isochrones. Notice that the total metal mass fraction Z is lower in the new isochrones, due to the different solar heavy element distribution.

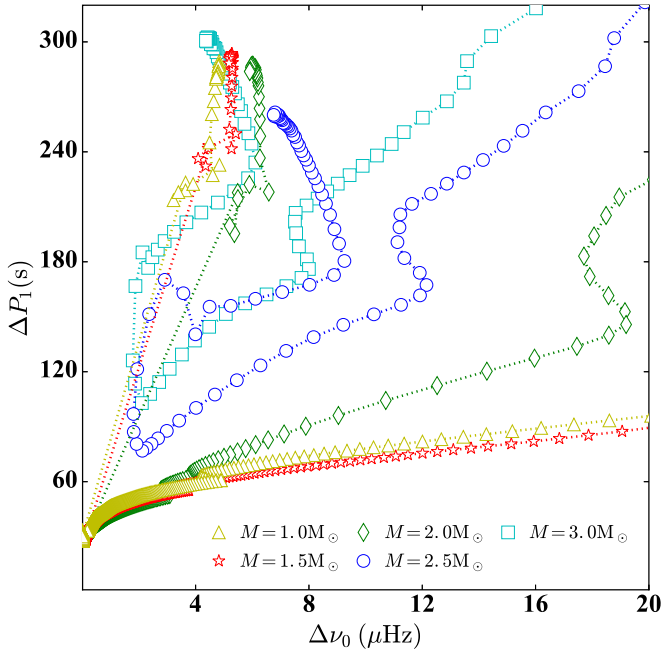

Figure 8. Asymptotic period spacing as a function of the large frequency separation for a set of five tracks with different masses and the same initial composition ($Y = 0.26$ and [Fe/H] $= -0.2$ dex).

The new isochrones have slightly hotter RGBs and TO. The core He-burning sequences are brighter for ages below 1 Gyr, and the HRD blue loops are generally more extended. Figure 10 enlarges the core He-burning portion of the isochrones for ages between 1 and 12 Gyr. The new isochrones have slightly fainter luminosities (by a few hundredth dex) during core He burning at these ages—mainly because of the new electron conduction opacities—and slightly hotter effective temperatures, as for the RGB. At 12 Gyr and [Fe/H]-1.55, the new isochrones show a cooler He-burning phase, because of the lower η used in the new calculations.

The main reason for the differences between these new BaSTI computations and the previous ones is the updated solar metal distribution and associated lower Z at a given [Fe/H]. However, the lower luminosity of the core He-burning phase at old ages is driven by the updated electron conduction opacities employed in these new calculations.

5.1. Pre-MS Isochrones

We have compared our new isochrones with independent calculations, considering separately pre-MS isochrones for low- and very low-mass stars, that can be calculated for a minimum age of just 4 Myr with our grid of models, whereas complete isochrones reaching the AGB phase or C-ignition start from an age of 20 Myr.

The pre-MS isochrones have been compared to results from the extensive database of Tognelli et al. (2011) and the "classic" models by Siess et al. (2000), as shown in Figure 11. These latter two calculations differ from ours with regard to some physics inputs. In particular, the Tognelli et al. (2011) isochrones have been calculated by adopting a different EOS and boundary conditions, while the Siess et al. (2000) isochrones have been computed with different low-temperature radiative opacities, EOS, and boundary conditions, and the initial deuterium abundance is about half the value used in our calculations. The reference solar metal mixture is different for each of the three sets of isochrones shown in the figure. The minimum evolving mass along the isochrones is equal to 0.1 $M_\odot$ for our and Siess et al. (2000) calculations, while it is equal to 0.2 $M_\odot$ for the Tognelli et al. (2011) models.

For the comparison, we have selected the Tognelli et al. (2011) calculations (which at fixed Z allow for various choices of Y, the deuterium mass fraction X_D, and mixing length) for $Z = 0.0175$, $Y = 0.265$, $X_D = 4 \times 10^{-5}$, $\alpha_{\rm ML} = 1.9$—very close to our initial solar chemical composition, the adopted initial deuterium mass fraction, and solar-calibrated mixing length—and the $Z = 0.02$ Siess et al. (2000) isochrones. We have considered ages equal to 4, 10, 15, 30, 50, and 100 Myr. The upper age limit is fixed by the largest age available for the Tognelli et al. (2011) calculations.

The agreement between our $Z = 0.0172$ ([Fe/H] $= 0.06$) and the Tognelli et al. (2011) isochrones is remarkable. They are almost indistinguishable, with appreciable differences appearing only for the lowest masses in common and the two youngest ages, where the Tognelli et al. (2011) isochrones are more luminous than ours at a given $T_{\rm eff}$. Differences with respect to the Siess et al. (2000) calculations are larger and more systematic, their isochrones being almost always brighter at fixed $T_{\rm eff}$ for stellar masses between $\sim$2.0–2.5 $M_\odot$ and $\sim$0.4 $M_\odot$.

5.2. MS and Post-MS Isochrones

Our complete isochrones have been compared with results from the recent PARSEC and MIST isochrones. We considered the nonrotating MIST isochrones and the PARSEC isochrones with VLM stellar models calculated with the "calibrated" boundary conditions, as described in Chen et al. (2014).

We considered our isochrones including convective core overshooting during the MS and atomic diffusion (the reference set (a) described in Table 3), since both effects are included in the MIST and PARSEC isochrones, although with varying implementations. Compared to our models, the nonrotating MIST isochrones have been calculated with different implementations of convective mixing (and include thermohaline mixing during the RGB), as well as different choices for the solar metal distribution, EOS, reaction rates, boundary conditions, mixing length theory formalism, and a lower value of the Reimers η parameter. Radiative levitation is neglected, and the efficiency of atomic diffusion during the MS is moderated by including a competing turbulent diffusive coefficient (see Choi et al. 2016 for details).

The PARSEC calculations have employed, compared to our new models, different choices for the low-temperature radiative opacities, electron conduction opacities, reaction rates, implementation of overshooting, boundary conditions, and a lower value of the Reimers parameter η. Atomic diffusion without radiative levitation is included, but switched off when the mass size of the outer convective region decreases below a given threshold (see Bressan et al. 2012 for details).

Figures 12 and 13 show selected isochrones for 30 Myr, 100 Myr, 1 Gyr, 3 Gyr, 5 Gyr, and 12 Gyr, and [Fe/H] $= 0.06$ and [Fe/H] $= -1.55$, respectively. They are shown together with PARSEC isochrones for the same ages, [Fe/H] $= 0.07$ and -1.59,[17] and MIST isochrones for the same ages and [Fe/H] as our isochrones.[18]

[17] Retrieved using the Web interface at http://stev.oapd.inaf.it/cgi-bin/cmd.
[18] Retrieved using the MIST Web interpolator at http://waps.cfa.harvard.edu/MIST/interp_isos.html.

Table 7
Main Differences Among the Physics Inputs and Solar Metal Mixture Adopted in Our Calculations and the Independent Calculations Discussed in This Section

Code	EOS	Reaction Rates	Opacity	Solar Mix
Tognelli et al. (2011) (Pre-MS)	OPAL (Rogers & Nayfonov 2002)	⋯	⋯	Asplund et al. (2005)
Siess et al. (2000) (Pre-MS)	Own calculations	Caughlan & Fowler (1988)	Low-T opacities (Alexander & Ferguson 1994) Electron conduction (Iben 1975)	Grevesse & Noels (1993)
PARSEC	⋯	JINA REACLIB (Cyburt et al. 2010)	Low-T opacities (Marigo & Aringer 2009) Electron conduction (Itoh et al. 2008)	⋯
MESA	Saumon et al. (1995) Rogers & Nayfonov (2002) MacDonald & Mullan (2012)	JINA REACLIB	⋯	Asplund et al. (2009)

Note. The symbol "—" denotes the same treatment as in our calculations.

Table 8
As Table 7, but for the Differences in the Treatment of Convective Mixing, Mass Loss, Mixing Length, and Outer Boundary Conditions

Code	Mixing	Reimers η and $\alpha_{\rm ML}$	Boundary Condition	Diffusion
Tognelli et al. (2011) (Pre-MS)	⋯	$\eta = 0.0$ $\alpha_{\rm ML} = 1.9$	Theoretical Model atmospheres	
Siess et al. (2000) (Pre-MS)	⋯	$\eta = 0.0$ $\alpha_{\rm ML} = 1.605$	Theoretical Model atmospheres	⋯
PARSEC	Proportional mean free path across border of all convective regions (Bressan et al. 1981)	$\eta = 0.2$ $\alpha_{\rm ML} = 1.74$	Gray $T(\tau)$ plus calibrated $T(\tau)$ for VLM models	Off when convective envelope mass below a threshold
MESA	Ledoux criterion, diffusive mixing, diffusive overshooting/semiconvective	$\eta = 0.1$ (RGB) $\eta = 0.2$ (AGB) $\alpha_{\rm ML} = 1.82$ (Henyey et al. 1965) formalism	Theoretical Model atmospheres	Moderated with diffusive mixing

The comparison with PARSEC isochrones displays a remarkable general agreement especially at lower [Fe/H], whereas at higher metallicity, the lower masses (which are still evolving along the pre-MS phase in the two youngest isochrones) are systematically discrepant compared to our models. The TO luminosities are only slightly different, especially at the three lowest ages, where the effect of different core overshooting prescriptions may play a role. The core He-burning phase is slightly overluminous compared to our models, and RGBs are slightly cooler compared to our [Fe/H] = 0.06 isochrones and slightly hotter compared to the [Fe/H] = −1.55 ones. Figures 14 and 15 enlarge the core He-burning portion of the isochrones for ages between 1 and 12 Gyr. The RGB of the PARSEC isochrones is cooler by less than 100 K compared to our models for [Fe/H] = 0.06, and hotter by less than 100 K at lower metallicity. The luminosity of the He-burning phase is only slightly larger (by a few hundredth dex) at both metallicities. Notice that at 12 Gyr the start of quiescent core He burning in our isochrones is at a hotter $T_{\rm eff}$ than in the PARSEC results, due to our choice of a larger Reimers parameter η.

The comparison with MIST isochrones yields similar results. There is an overall good agreement for the MS, TO, and subgiant-branch (SGB) phases, and also in the regime of the lowest masses, still evolving along the pre-MS at the youngest ages. The He-burning phase of MIST isochrones is generally overluminous, and RGBs are systematically redder at [Fe/H] = 0.06, and with a different slope at [Fe/H] = −1.55. Figures 14 and 15 show RGBs over 100 K cooler than our models at [Fe/H] = 0.06, and slightly larger core He-burning luminosities, like in the comparison with PARSEC. Also, in comparison with MIST isochrones, at 12 Gyr, the start of quiescent core He burning in our isochrones is at a hotter $T_{\rm eff}$, again due to our choice of a larger Reimers parameter η.

6. Comparisons with Data

In this section, we present the results of some tests performed to assess the general consistency of our new models and isochrones with constraints coming from eclipsing binary analyses, stars with asteroseismic mass determinations, and star clusters. The isochrones used in these comparisons include convective core overshooting during the MS for the appropriate age range and ignore atomic diffusion during the MS (set (b) of models described in Table 3), if not otherwise specified.

6.1. Binaries

We first consider masses and radii for the pre-MS detached eclipsing binary (DEB) systems compiled by Stassun et al. (2014) and Simon & Toraskar (2017), covering a mass range

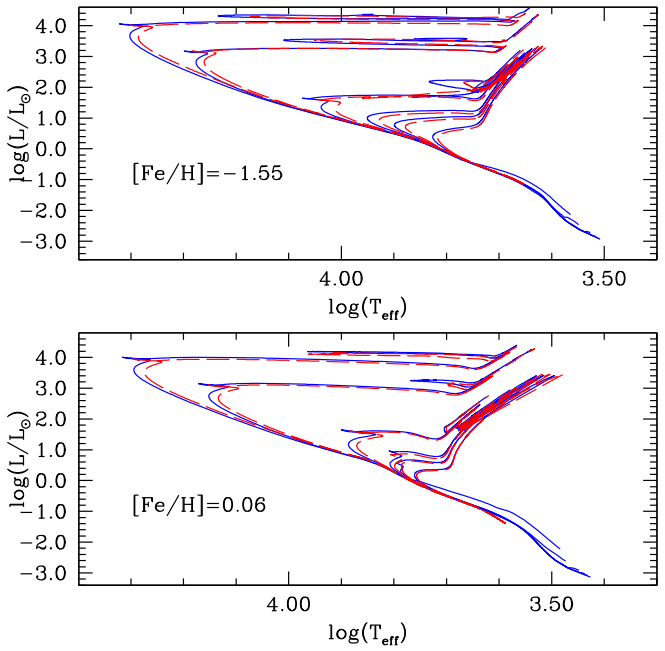

Figure 9. Comparison of our isochrones for [Fe/H] = 0.06 and [Fe/H] = −1.55 (solid lines) with the older BaSTI isochrones for [Fe/H] = 0.06 and [Fe/H] = −1.49 (dashed lines), and ages equal to 30 Myr, 100 Myr, 1 Gyr, 3 Gyr, 5 Gyr, and 12 Gyr, respectively (see the text for details).

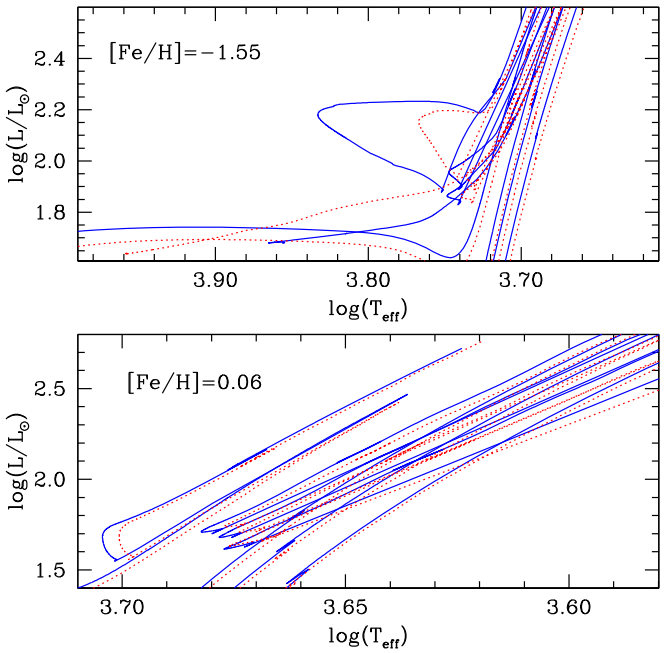

Figure 10. As Figure 9, but showing the core He-burning region for ages between 1 and 12 Gyr. The older BaSTI isochrones are displayed as dotted lines.

between $0.2\,M_{\odot}$ and $4.0\,M_{\odot}$. We assume an initial [Fe/H] = 0.06 (overall consistent with the few available spectroscopic estimates; see Stassun et al. 2014), and consider a minimum age of 4 Myr, the lowest possible value with our model grid. We do not aim to find a best-fit solution for all of the systems, just at least one isochrone that matches simultaneously the mass and radius of both components for each system within the errors, to denote a general consistency between models and observations.

This test is relevant for the general adequacy of both boundary conditions and $\alpha_{\rm ML}$ values employed in the calculations, given the extreme sensitivity of pre-MS tracks to the combination of these two inputs. It is, however, worth noticing that the lack of model-independent age estimates prevent this type of test from providing very stringent constraints on the models.

We found 13 systems in the age range covered by our pre-MS isochrones, displayed in a mass–radius (MR) diagram in Figure 16. In the case of all these systems, our isochrones can match both components within the quoted 1σ error bars with a single age value, varying between 5 and 60 Myr within the entire sample of DEBs.

The next test involves low-mass MS models. The existence of a disagreement between theoretical and observational MR relationships for low-mass stars has been recognized for some time now, with model radii typically 10%–20% smaller than observations for a fixed mass (see, e.g., Torres et al. 2010 for a review). Here we examine first the level of agreement between the observed and theoretical MS low-mass MR relationship by comparing our grid of models with data from DEB systems that host components with $M < 0.8\,M_{\odot}$, as compiled by Feiden & Chaboyer (2012). This compilation includes systems with quoted random uncertainties in both mass and radius below 3%. As for the pre-MS case, the requirement for the models is that they are able to match the position of both system components in the MR diagram for a single value of the age.

We assume that all DEBs have metallicity around solar (see also Feiden & Chaboyer 2012 for spectroscopic metallicity estimates for a few of the systems in their compilation) and split the sample into two subsamples. The first one is made of systems with both components essentially on the ZAMS, displayed in Figure 17, together with isochrones of ages equal to 1 Gyr and 12 Gyr respectively, and [Fe/H] = 0.06. We also show a 12 Gyr isochrone for [Fe/H] = −0.40 to highlight the insensitivity of the theoretical MR relationship to metallicity, when the mass is below $\sim 0.7\,M_{\odot}$.

Isochrones appear to match all systems reasonably well, without a clear major systematic discrepancy in radius at fixed mass. The effect of age is very small for this mass range. If we denote with ΔR the difference $R_{\rm obs} - R_{\rm theory}$ between observed and predicted radii for an object with observed mass M, we find an average $\Delta R/R_{\rm obs} = 0.02 \pm 0.03$ assuming an age of 12 Gyr for all systems, and an average $\Delta R/R_{\rm obs} = 0.04 \pm 0.03$ for an age of 1 Gyr (see the inset of Figure 17). These average differences are consistent with typical systematic errors on empirical radius estimates—of the order of 2%–3%—as determined by Windmiller et al. (2010) in their reanalysis of the DEB system Gu Boo.

The second subsample (see Figure 18) includes systems with one or both components evolved off the ZAMS. We impose an upper limit of 13.5 Gyr to their ages, to match the cosmological constraint. The major discrepancy here is for UV Psc, whereby one component is matched by the 9 Gyr isochrone, whereas the less massive one appears older than 13.5 Gyr. A minor discrepancy also affects IM Vir, with the lower-mass component appearing slightly older than the companion.

On the whole, there is no major systematic discrepancy between models and observed MR relationships, although there are clear mismatches for a few cases, as found also by Feiden & Chaboyer's (2012) analysis. Another example of a mismatch is

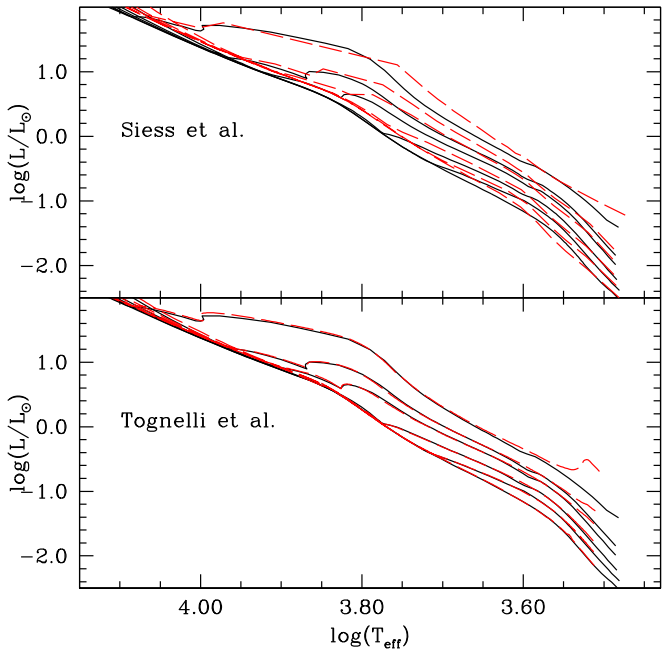

Figure 11. Comparison of our pre-MS isochrones (solid lines) with the Siess et al. (2000) and Tognelli et al. (2011) results (dashed lines in the top and bottom panels, respectively) for a metallicity around solar and ages equal to 4, 10, 15, 30, 50, and 100 Myr (see the text for details).

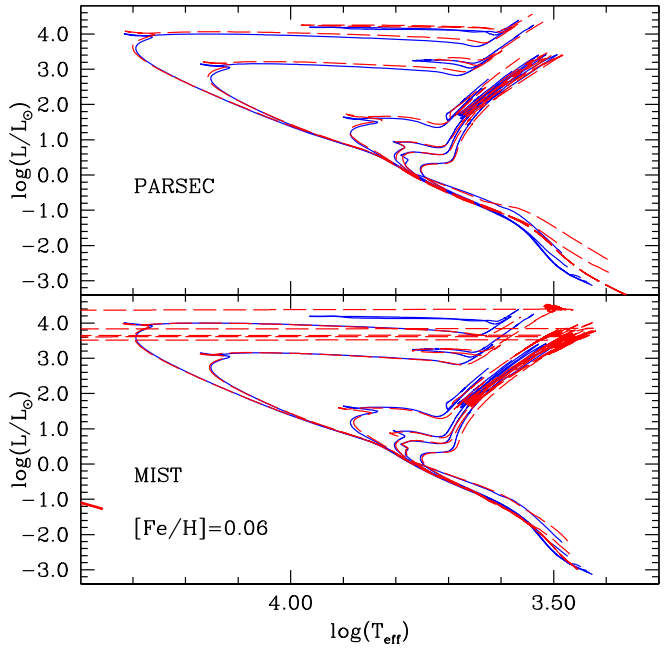

Figure 12. Comparison of our complete isochrones for [Fe/H] = 0.06 (solid lines) with the PARSEC and MIST results (dashed lines in the top and bottom panels, respectively) and ages equal to 30 Myr, 100 Myr, 1 Gyr, 3 Gyr, 5 Gyr, and 12 Gyr (see the text for details).

the M-dwarf system (both components with masses around 0.4 $M_{\odot}$) KELT J041621–620046 studied very recently by Lubin et al. (2017) and shown in Figure 17. Our isochrones give radii systematically lower by ∼20% than observed for both components (as with all other models employed by Lubin et al. 2017). The commonly accepted explanation for these mismatches (see, e.g., Feiden & Chaboyer 2012; Lubin et al. 2017, and references therein) involves the effects of large-scale magnetic fields that suppress convective motions and increase

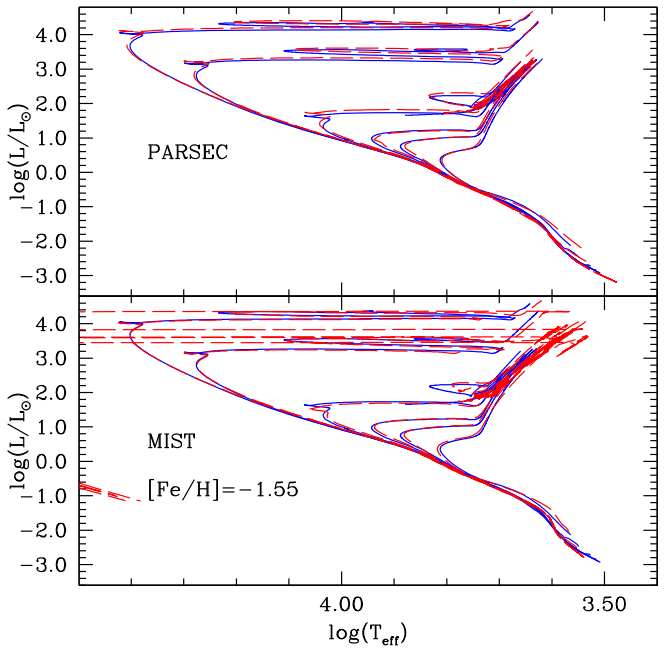

Figure 13. As Figure 12 but for [Fe/H] = −1.55 (see the text for details).

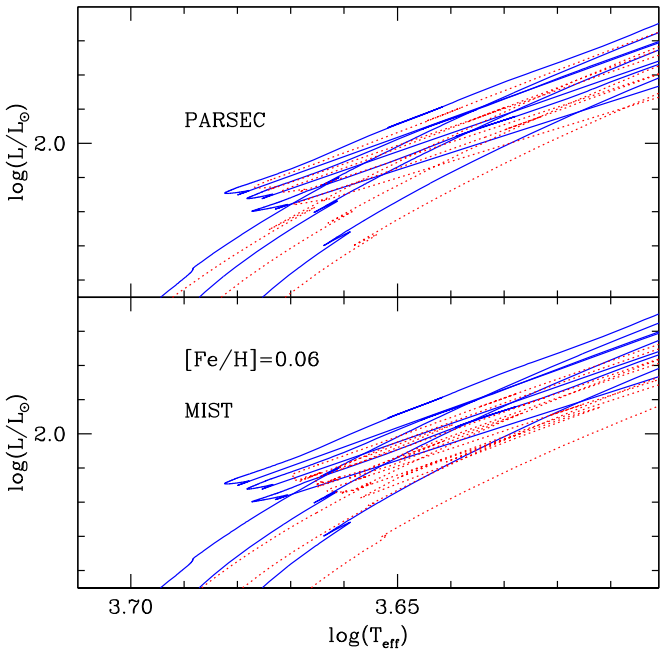

Figure 14. As Figure 12, but showing the core He-burning region for ages between 1 and 12 Gyr. The MIST and PARSEC isochrones are displayed as dotted lines.

the total surface coverage of starspots. This causes a reduction in the total energy flux across a given surface within the star, forcing the stellar radius to inflate and ensuring flux conservation. For the sake of comparison, we also show in Figure 17 a 50 Myr, [Fe/H] = 0.06 pre-MS isochrone that would match within the error bars the position of the KELT J041621–620046 components in the MR diagram, in case these objects were actually pre-MS stars.

The next comparison involves the DEB system KIC 8410637, studied by Frandsen et al. (2013). It contains an MS and an RGB star, and is another good test for the calibration of convection in the models. Figure 19 compares

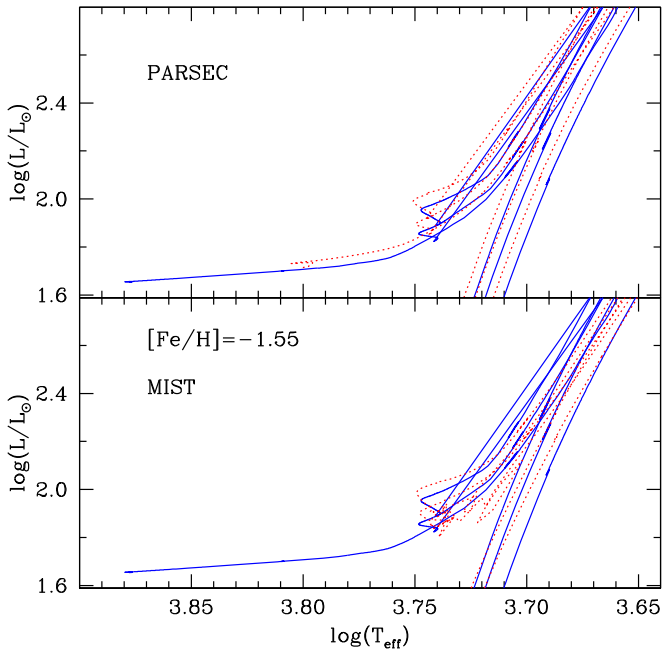

Figure 15. As Figure 14, but for [Fe/H] = −1.55.

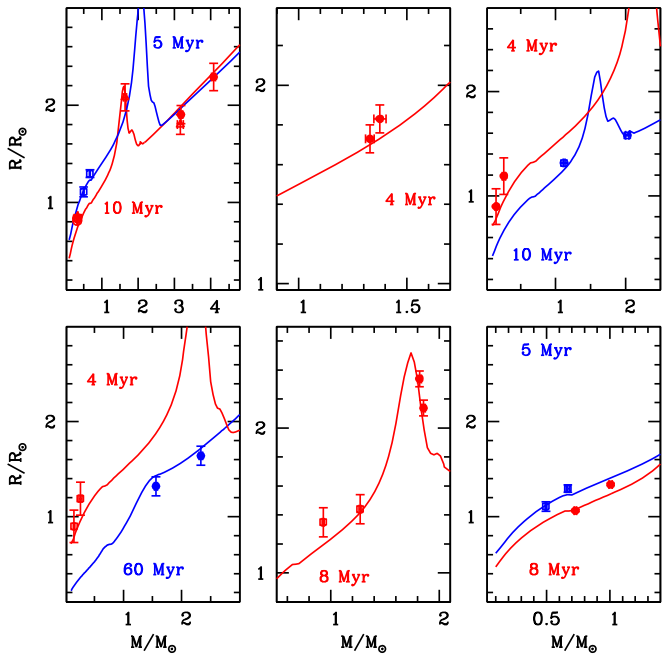

Figure 16. Comparison in the mass–radius diagram between our pre-MS isochrones and a sample of pre-MS DEB systems (see the text for details). Notice the local maximum of the radius displayed by the 4, 5, 8, and 10 Myr isochrones, corresponding to C and N abundances attaining their equilibrium abundances.

observations and isochrones in the MR diagram. When considering isochrones for [Fe/H] = 0.06, consistent with the spectroscopic estimate by Frandsen et al. (2013), we find that an age of 2.5 Gyr matches very well the position of the two components (a similar result was found by Frandsen et al. 2013 using PARSEC isochrones).

The last DEB systems compared to our models are four objects from the Claret & Torres (2017) compilation. Their spectroscopic metallicity is consistent within errors with [Fe/H] = −0.40; the masses of the various components range between ∼1.4 $M_{\odot}$ and

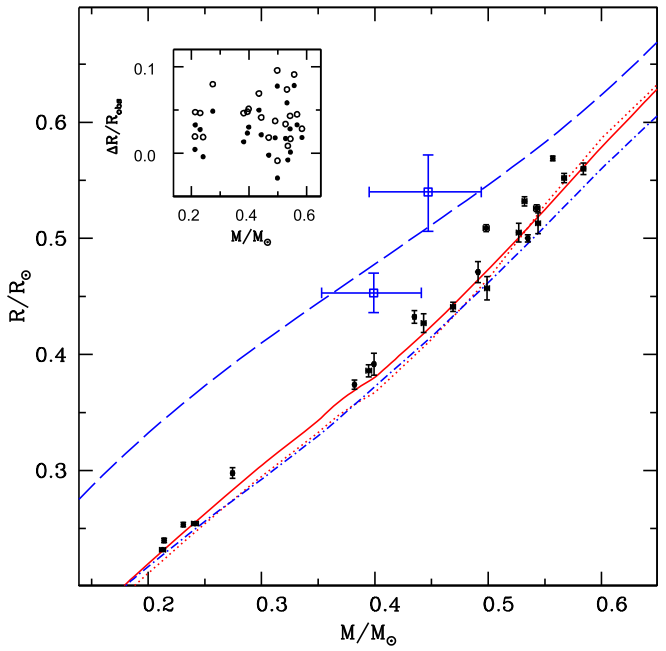

Figure 17. Comparison in the MR diagram between our 1 Gyr (dashed dotted line) and 12 Gyr (solid line) [Fe/H] = 0.06 isochrones, and a subsample of Feiden & Chaboyer (2012) DEB systems whose components are found to be evolving on the ZAMS. The dotted line denotes a 12 Gyr old [Fe/H] = −0.40 isochrone, showing the almost negligible effect of metallicity variations when the mass is below ∼0.7 $M_{\odot}$. Open squares denote the components of the system KELT J041621–62004. The dashed line displays a 50 Myr, [Fe/H] = 0.06 pre-MS isochrone. The inset shows the run of the relative radius differences (observations – theory) $\Delta R/R_{\rm obs}$ with the mass of the systems' components (except for the system KELT J041621–62004) for an age of 1 Gyr (open circles) and 12 Gyr (filled circles—see the text for details).

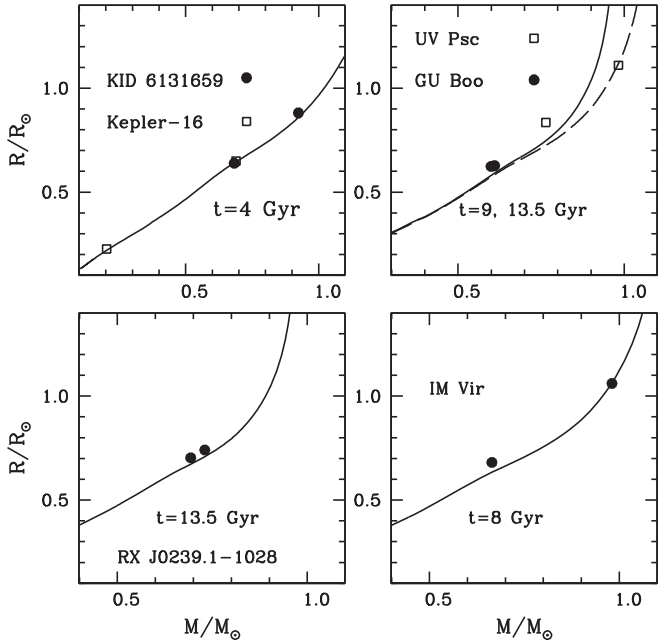

Figure 18. As Figure 17, but for Feiden & Chaboyer (2012) DEB systems with at least one component evolved off the ZAMS.

∼4.2 $M_{\odot}$, and they are evolving along either the RGB or core He-burning phase. Figure 20 shows the comparison of their MR diagrams with theoretical isochrones for [Fe/H] = −0.40, which are able to match simultaneously both components (within their mass and radius error bars) in all four systems for the labelled

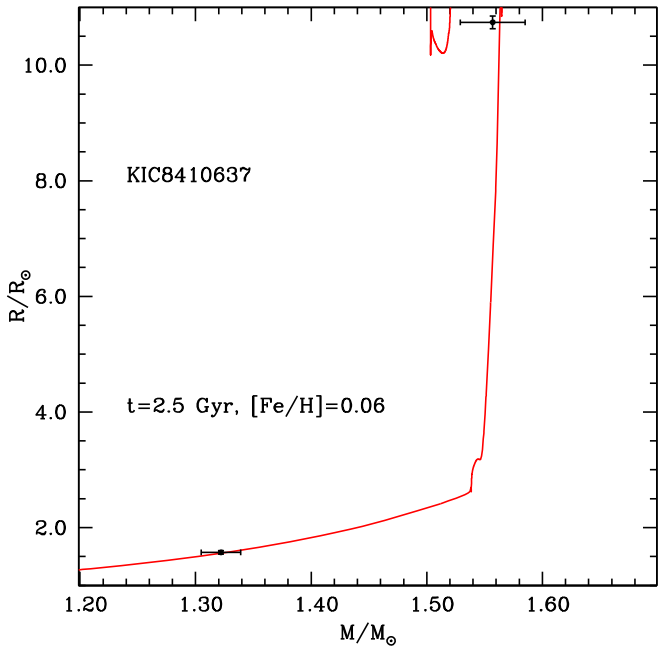

Figure 19. As Figure 17, but for the components of the KIC 8410637 system (see the text for details).

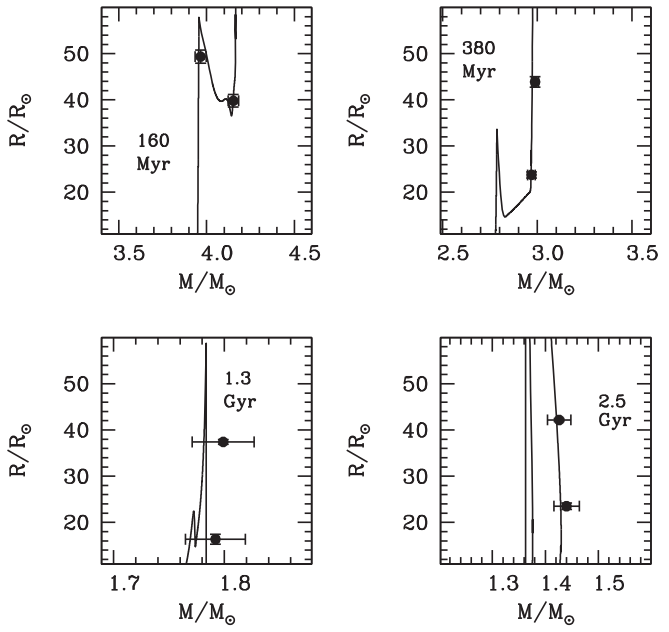

Figure 20. As Figure 17, but for the components of the OGLE-LMC-ECL-06575, OGLE-LMC-ECL-09660, OGLE-LMC-ECL-15260, and OGLE-LMC-ECL-03160 systems, moving clockwise from the top-left panel (see the text for details).

ages, with our choices of MS core overshooting efficiency and mixing length.

Finally, we compare the mass–luminosity relationship predicted by our low-mass models in the V and K bands, with the data presented by Delfosse et al. (2000), based mainly on visual and interferometric pairs. We display in Figure 21 the observational data together with three isochrones with [Fe/H] = 0.06 and ages equal to 300 Myr, 1 Gyr, and 10 Gyr respectively (solid lines), plus two 10 Gyr isochrones with [Fe/H] = −0.40 and [Fe/H] = 0.45, respectively (dashed lines).

First of all, as also noted by Delfosse et al. (2000), the V-band data show a large dispersion at fixed M, with models matching a sort of upper envelope of the data. The K-band data are much tighter and in very good general agreement with the [Fe/H] = 0.06 models, even though the sample is smaller than for the V band. It is interesting to consider the two objects highlighted by the dotted lines. They have estimates of both V and K absolute magnitudes; in the K band, the agreement with theory for [Fe/H] = 0.06 (or higher) is essentially perfect, whereas in the V band, the data are clearly underluminous compared to the models. The fact that the V-band diagram is much more sensitive to the exact metallicity of the sample (as shown by the dashed lines in the figure) suggests that [Fe/H] may play a role in explaining this dispersion. The [Fe/H] = 0.45 isochrone is underluminous at fixed mass compared to the [Fe/H] = 0.06 one, but still cannot explain the full dispersion of the data.

Figure 22 displays a similar comparison with the more recent mass–luminosity empirical data by Benedict et al. (2016). Also, in this case, the dispersion in the V band is larger than that in the K band. In the K band (which is weakly sensitive to chemical composition), the agreement with theory is again generally quite good, apart from the cluster of objects with mass around 0.6 $M_{\odot}$ that appear somewhat underluminous with respect to the models, irrespective of the adopted metallicity between [Fe/H] = −0.4 and 0.45.

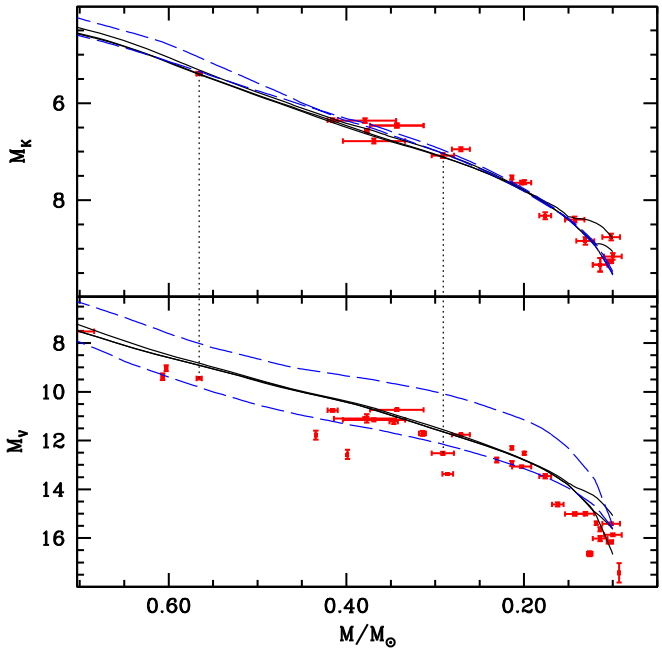

Figure 21. Comparison of theoretical and observed mass–luminosity relationships in the V and K bands for a sample of low-mass stars from Delfosse et al. (2000). Filled symbols with error bars display the data, while solid lines correspond to three isochrones with [Fe/H] = 0.06 and ages equal to 300 Myr, 1 Gyr, and 10 Gyr respectively. The dashed lines show 10 Gyr isochrones with [Fe/H] = −0.40 (brighter at fixed mass compared to the [Fe/H] = 0.06 isochrones) and [Fe/H] = 0.45, respectively. Dotted lines highlight two objects that are inconsistent with the models in the V band, but fully consistent in the K band (see the text for details).

6.2. Stars with Asteroseismic Mass Determinations

A recent study by Tayar et al. (2017) has provided a sample of over 3000 RGB stars with $T_{\rm eff}$, mass (determined from asteroseismic scaling relations), surface gravity, [Fe/H], and

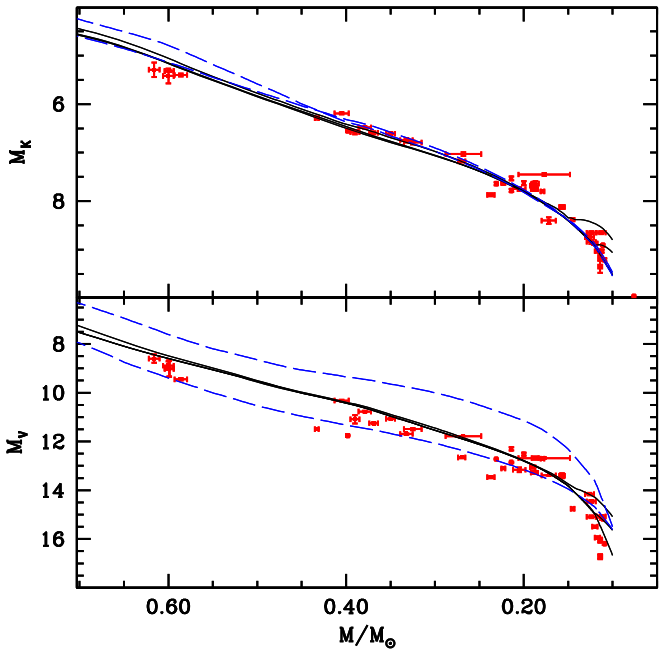

Figure 22. As Figure 21, but for the observed mass–luminosity relationships from Benedict et al. (2016; see the text for details).

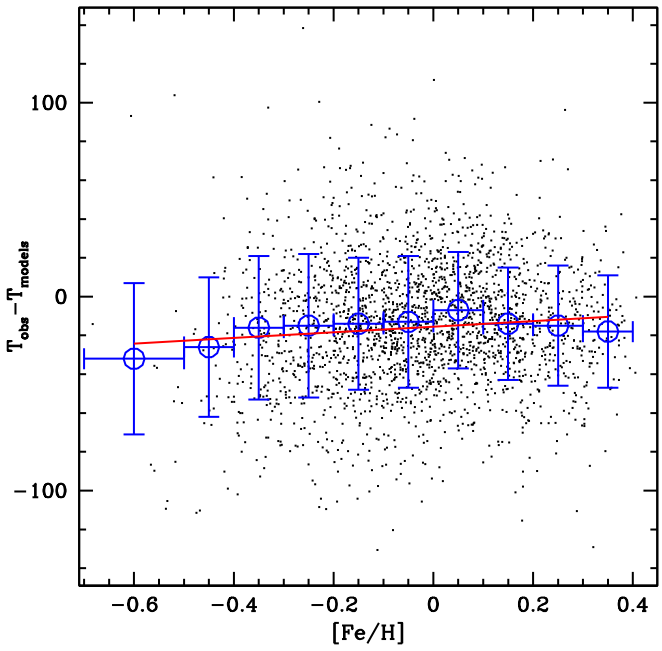

Figure 23. ΔT as a function of [Fe/H] (dots) for RGB stars with asteroseismic mass determinations from Tayar et al. (2017) and $[\alpha/\mathrm{Fe}] < 0.07$. Open circles with error bars denote the mean values of ΔT in specific metallicity bins, while the solid line displays a linear fit to the binned data. Vertical error bars denote the 1σ dispersion around the mean values of ΔT in each bin, whereas the horizontal error bars denote the width of the [Fe/H] bins.

α-enhancement ($[\alpha/\mathrm{Fe}]$) determinations from the updated APOGEE-*Kepler* catalog. These stars cover a $\log(g)$ range between $\sim$3.3 and 1.1 (in cgs units), and $T_{\rm eff}$ between $\sim$5200 and 3900 K, with the bulk of the stars having [Fe/H] between ~-0.7 and $\sim+0.4$ dex, and a maximum α-enhancement typically around 0.25 dex. This sample allows empirically determined $T_{\rm eff}$ values (calibrated on the González Hernández & Bonifacio 2009 temperature scale) to be compared with theoretical models of the appropriate chemical composition, which are very sensitive to the treatment of the superadiabatic layers, hence to the calibration of $\alpha_{\rm ML}$.

In our comparison, we have considered only stars with $[\alpha/\mathrm{Fe}] < 0.07$ (this upper limit corresponds to approximately three to five times the quoted 1σ error on $[\alpha/\mathrm{Fe}]$), but an upper limit closer to zero does not change our results. We have calculated the differences $\Delta T \equiv T_{\rm obs} - T_{\rm models}$ between the observed and theoretical $T_{\rm eff}$ for each individual star by interpolating linearly in mass, [Fe/H], and $\log(g)$ among our models to determine the corresponding theoretical $T_{\rm eff}$. The ΔT values for [Fe/H] larger than ~-0.7 dex have been collected in 10 [Fe/H] bins with a total width of 0.10 dex, apart from the most metal-poor one, which has a width of 0.20 dex, due to the smaller number of stars populating that metallicity range. We have then performed a linear fit to the mean ΔT values of each bin, and derived a slope equal to 14 ± 11 K dex^{-1}, which is statistically different from zero at much less than 2σ (see Figure 23). The average ΔT is equal to just -14 K, with a 1σ dispersion of 34 K. This small offset between models and observations is well within the error on the González Hernández & Bonifacio (2009) $T_{\rm eff}$ calibration (the quoted average error on their RGB $T_{\rm eff}$ scale is $\leqslant 76\ K$).

6.3. Star Clusters

The following comparisons with CMDs of a sample of Galactic open clusters and one globular cluster (with solar-scaled initial metal distribution) provide additional tests of the reliability of our evolutionary tracks/isochrones plus the adopted BCs. In all of these comparisons, we have included the effect of extinction according to the standard Cardelli et al. (1989) reddening law, with $R_V \equiv A_V/E(B-V) = 3.1$.

Figure 24 displays the $BVJHK_s$ CMDs (JHK_s from 2MASS photometry) for Hyades members taken from Röser et al. (2011) and Kopytova et al. (2016), which reach the VLM star regime, down to $\sim 0.2 M_\odot$. We have calculated absolute magnitudes by applying the secular parallaxes determined by Röser et al. (2011). The average parallax of these objects is in agreement with the average value of 103 probable members of the Hyades from the *Gaia* data release 1, as given by *Gaia* Collaboration et al. (2017), within the quoted errors. We also display color and absolute magnitude error bars (the error bars on the absolute magnitudes also account for the contribution of the parallax errors), given that color errors often are non-negligible along the MS.

The cluster CMDs are compared with our $t = 600$ and 800 Myr, $[\mathrm{Fe/H}] = 0.06$ isochrones—close to spectroscopic estimates $[\mathrm{Fe/H}] = 0.14 \pm 0.05$ (Cayrel de Strobel et al. 1997) and $[\mathrm{Fe/H}] = 0.10 \pm 0.01$ (Taylor & Joner 2005)—assuming $E(B-V) = 0$, consistent with the results of Taylor (2006). The age range bracketed by these two isochrones is representative of the range of ages estimated for this cluster, as recently debated in the literature (see, e.g., Perryman et al. 1998; Brandt & Huang 2015 and references therein).

The theoretical isochrones follow well the observed MS down to the faintest limit, apart from the *JH* diagram, which shows a systematic offset due to the *H*-band BCs, although the models are still consistent with the data within the associated error bars.

Optical CMDs of NGC 2420 (Anthony-Twarog et al. 1990) and M67 (Sandquist 2004) are shown in Figure 25 compared to isochrones with $t = 2.5$ Gyr and $[\mathrm{Fe/H}] = -0.40$ in the case of NGC 2420, and $t = 4$ Gyr and $[\mathrm{Fe/H}] = 0.06$ for M67,

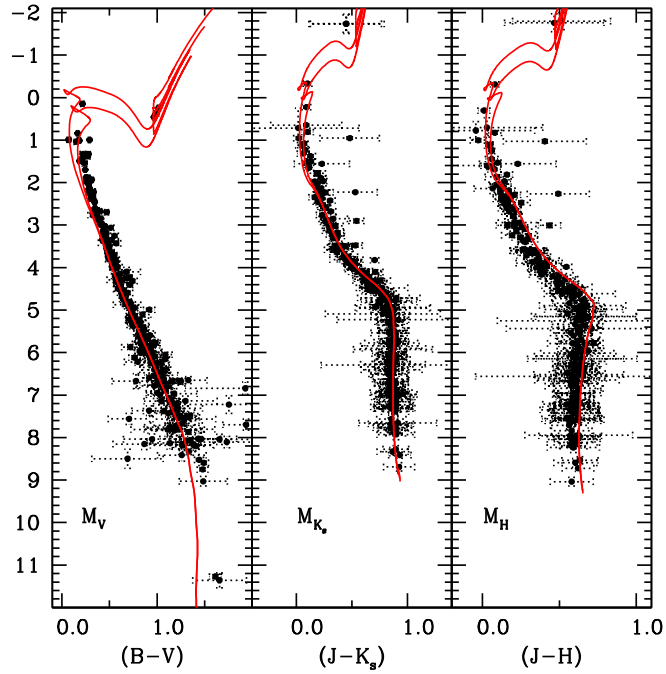

Figure 24. Comparison between our 600 and 800 Myr, [Fe/H] = 0.06 isochrones, and three Hyades CMDs, corrected for the secular parallaxes determined by Röser et al. (2011)—see the text for details.

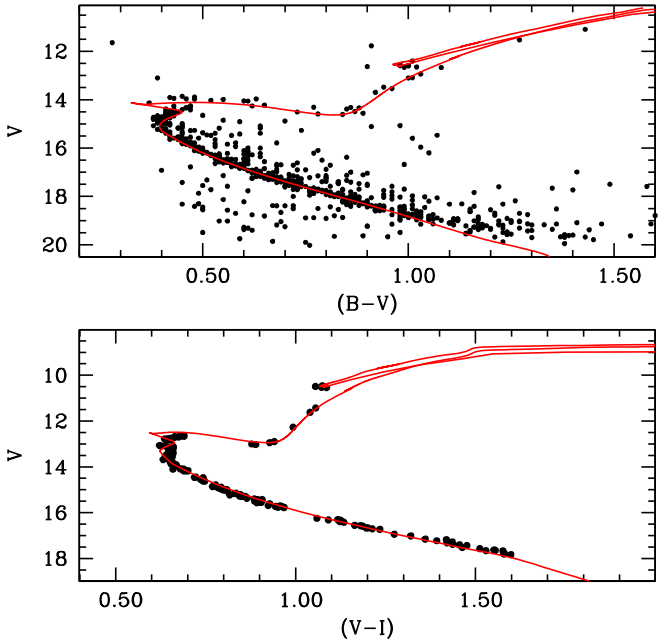

Figure 25. Optical CMDs for NGC 2420 (top panel) and M67 (bottom panel). Our isochrones with [Fe/H] = −0.40, t = 2.5 Gyr, $(m-M)_0$ = 11.95, and $E(B-V)$ = 0.06 (top panel) and [Fe/H] = 0.06, t = 4 Gyr, $(m-M)_0$ = 9.64, and $E(B-V)$ = 0.02 (bottom panel) are also shown (see the text for details).

respectively. These metallicities are consistent with [Fe/H] = −0.44 ± 0.06 (NGC 2420) and [Fe/H] = 0.02 ± 0.06 (M67) quoted by Gratton (2000). The isochrones have been shifted to account for distance moduli and reddenings $(m-M)_0$ = 11.95, $E(B-V)$ = 0.06 for NGC 2420, and $(m-M)_0$ = 9.64, $E(B-V)$ = 0.02 for M67. These pairs of values are consistent with the reddening estimates by Twarog et al. (1997) and the MS-fitting distance moduli (using dwarfs with accurate *Hipparcos* parallaxes) by Percival & Salaris (2003), within their error bars.

The values of the mass evolving at the TO for the NGC 2420 and M67 isochrones are ∼1.3 $M_\odot$ and ∼1.2 $M_\odot$, respectively, in the mass range where the size of the overshooting region is decreased down to zero from the standard value of $0.2H_p$. The shape of the TO region, which is sensitive to the extent of the overshooting region, is well traced by the isochrones for both clusters, lending some support to our prescription for the reduction of size of the overshooting region with mass.

One can notice also how, in addition to the MS (apart from the faintest end of the NGC 2420 MS), the RGB, SGB and red clump sequences are also nicely matched by the isochrones.

The next object compared to our isochrones is the old and super metal-rich open cluster NGC 6791. At the supersolar metallicity of this object, BCs are bound to be more uncertain, because inaccuracies in atomic and molecular opacity data entering the model spectra calculations are greatly enhanced in this metallicity regime.

For this cluster, we take advantage of the analysis by Brogaard et al. (2011, 2012) of two DEB systems, which provide estimates of $E(B-V) = 0.16 \pm 0.025$, $(m-M)_V = 13.51 \pm 0.06$, and [Fe/H] = +0.29 ± 0.03(random) ± 0.07(systematic), with this last value in agreement, within the errors, with spectroscopic estimates by Origlia et al. (2006) and Carraro et al. (2006), but lower than [Fe/H] = +0.47 ± 0.04 determined by Gratton et al. (2006).

Figure 26 displays the MR diagram for the four components (the primary component of V20 is in the TO region of the CMD; the other components are increasingly fainter MS stars) of these two DEB systems (named V18 and V20 in Brogaard et al. 2011) including the 1σ and 3σ error bars, together with two theoretical isochrones for [Fe/H] = 0.30, with and without the inclusion of atomic diffusion,[19] and ages of 8.5 Gyr and 9.0 Gyr, respectively.

As for the isochrones discussed by Brogaard et al. (2012), it is not possible to match perfectly the MR diagram of these EBs with theoretical isochrones. Those shown in Figure 26 represent the best compromise to match the data for the four DEB components, within their errors.

Figure 27 places the same isochrones of the DEB comparison in optical *BVI* CMDs together with the cluster photometry, corrected for differential reddening, by Brogaard et al. (2012). We have displayed only stars with good quality photometry, i.e., we have considered only objects with photometric reduction yielding a sharp index between −0.4 and +0.4, and a chi index between 0.9 and 1.2. The isochrones have been shifted in color for a reddening $E(B-V)$ = 0.16, and vertically for $(m-M)_V$ = 13.52 (the isochrone with diffusion) and $(m-M)_V$ = 13.54 (the isochrone without diffusion), respectively. These distance moduli, both consistent with the result from the DEB analyses, allow the V-band magnitude of the observed red clump stars to be matched with the core He-burning portion of the isochrones. The overall comparison is better in the *BV* CMD, where the RGB location and slope are reasonably reproduced, as well as the TO−SGB −upper-MS sequence. The TO region is matched better by the isochrone including atomic diffusion. In *VI*, the match is worse

[19] When diffusion is efficient, the quoted isochrone [Fe/H] corresponds to the initial value, which is also the one reinstated along the RGB by the deepening convection, after the first dredge-up is completed. Notice that spectroscopic measurements of [Fe/H] in NGC 6791 and the Galactic globular cluster Rup 106, discussed later, have been obtained for bright RGB stars.

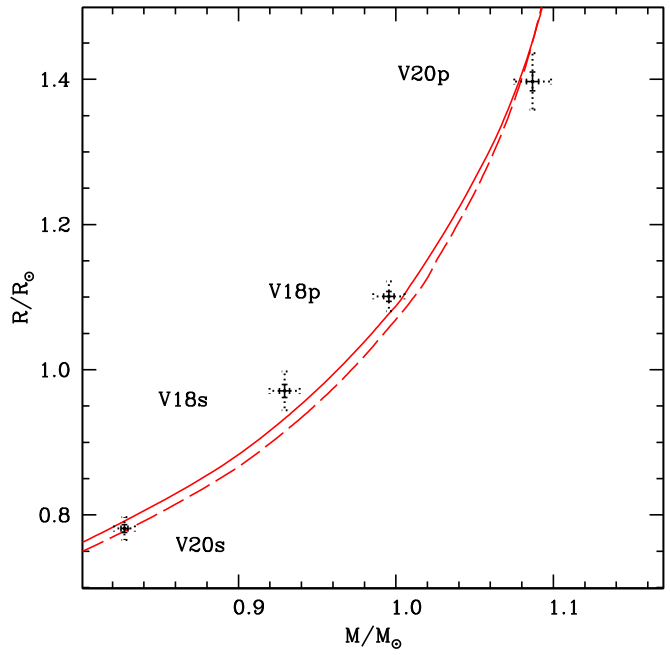

Figure 26. Comparison in the mass–radius diagram between the primary and secondary components of the DEB systems V18 and V20 in NGC 6791, and our [Fe/H] = 0.30 isochrones with $t = 8.5$ Gyr including atomic diffusion (solid line), and $t = 9.0$ Gyr without atomic diffusion (dashed line).

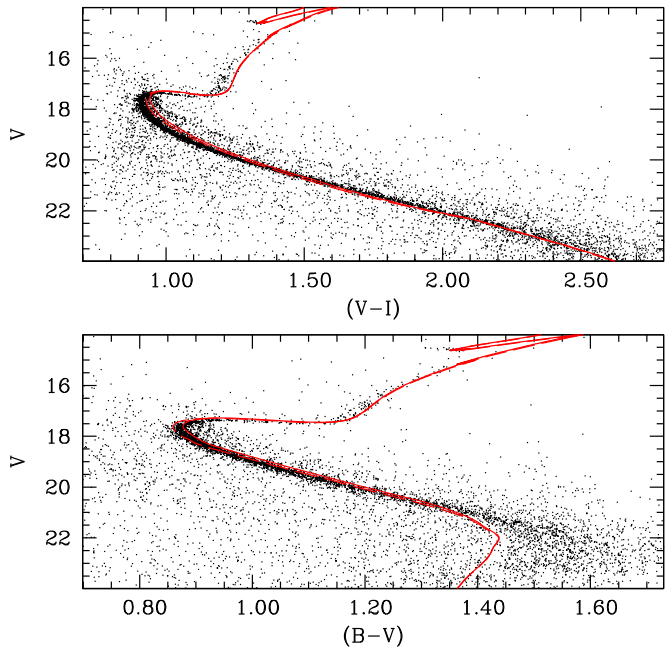

Figure 27. *BVI* CMDs for NGC 6791, compared to the same isochrones of Figure 26. The isochrones have been shifted in magnitude and colors by $(m - M)_V = 13.52$ (isochrone with diffusion, shown as a solid line) and $(m - M)_V = 13.54$ (isochrone without diffusion, shown as a dashed line), and $E(B - V) = 0.16$ (see the text for details).

overall. The RGB of the isochrones is redder than observed; the TO−SGB region is less well reproduced than in *BV*, although a lower MS is better matched.

As a last object, we have considered the low-mass (total actual mass lower than 10^5 $M_\odot$; see Villanova et al. 2013) outer halo Galactic globular cluster Rup 106, whose stars display a solar-scaled metal distribution, without the O–Na and C–N abundance

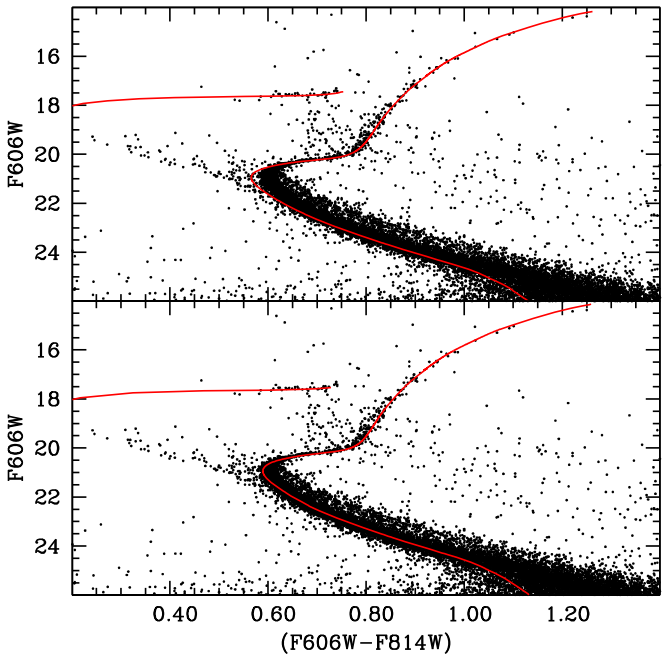

Figure 28. Optical *HST*/ACS CMD for Rup 106, compared to our ZAHB sequences and isochrones with [Fe/H] = −1.55, $t = 12.5$ Gyr, $(m - M)_0 = 16.69$, $E(B - V) = 0.18$, and no atomic diffusion (top panel), and $t = 11.5$ Gyr $(m - M)_0 = 16.66$, $E(B - V) = 0.18$, and including atomic diffusion (lower panel—see the text for details).

anticorrelations common in other Galactic globular clusters (Villanova et al. 2013). Figure 28 shows the cluster optical CMD in the *HST*/ACS camera photometric system (Dotter et al. 2011), together with isochrones for [Fe/H] = −1.55—close to the mean value [Fe/H] = −1.47 ± 0.02 determined spectroscopically by Villanova et al. (2013)—$t = 12.5$ Gyr (without atomic diffusion) and $t = 11.5$ Gyr (including atomic diffusion), and ZAHB sequences (obtained from models with and without diffusion, respectively) for the same metallicity. A reddening $E(B - V) = 0.18$ and distance modulus $(m - M)_0 = 16.66$, for isochrones and ZAHB models with diffusion, and $(m - M)_0 = 16.69$, for isochrones and ZAHB models without diffusion, have been applied to the models. The distance moduli have been fixed by matching the theoretical ZAHB sequences to the lower envelope of the observed HB.

The isochrones follow well the observed CMD. The TO region is better matched by the isochrone including atomic diffusion. Increasing the age of the isochrone without diffusion to make its TO redder does not improve the match with observations, because the model SGB would become fainter than the observed one.

7. Conclusions

In this paper, we have presented a comprehensive overview of the updated BaSTI models, discussing the change in physics inputs compared to the previous BaSTI calculations, including comparisons with recent independent stellar model and isochrone databases, and a host of observational tests. Improving upon the previous BaSTI release, this new library increases significantly the number of available metallicities, includes the VLM regime, accounts consistently for the pre-MS evolution in the isochrone calculations, and also provides the asteroseismic properties of the models.

Our new models/isochrones are able to match several sets of independent observational constraints that involve pre-MS stars and objects in more advanced evolutionary phases, either single, in DEBs, or in star clusters. We believe that this updated BaSTI release will be an important tool to investigate field, cluster, Galactic, and extragalactic stellar populations.

We make publicly available the entire database of models and isochrones through two dedicated web sites at the following URL addresses: http://basti-iac.oa-abruzzo.inaf.it and https://basti-iac.iac.es. Here, we provide tables of the stellar evolutionary tracks and asteroseismic properties of our grid of stellar evolution calculations plus isochrones, in several photometric systems. We can also provide, upon request, additional calculations and both evolutionary and asteroseismic outputs for stellar masses not in our standard grids.

In the near future, we will set up a Web interface to enable interpolations in metallicity within the available track and isochrone grids, as well as the calculations of isochrones and luminosity functions for any specified age.

The next paper of this series will present α-enhanced and α-depleted models and isochrones, which are particularly suited to study stellar populations in globular clusters and dwarf galaxies.

S.C. acknowledges partial financial support from PRIN-INAF2014 (PI: S.C.) and from "Progetto Premiale" MIUR *MITIC* (PI: B.G.). Funding for the Stellar Astrophysics Centre is provided by The Danish National Research Foundation (grant agreement No. DNRF106). V.S.A. acknowledges support from the Villum Foundation (research grant 10118). This research has been supported by the Spanish Ministry of Economy and Competitiveness (MINECO) under the grant SEV-2011-0187 (A.A. & S.L.H.). We warmly thank F. Castelli for her helpful comments and suggestions. We warmly thank the referee for a prompt and extremely helpful report, which greatly improved the presentation of our results.

ORCID iDs

Sebastian L. Hidalgo https://orcid.org/0000-0002-0002-9298
Santi Cassisi https://orcid.org/0000-0001-5870-3735
Alessio Mucciarelli https://orcid.org/0000-0001-9158-8580
Antonio Aparicio https://orcid.org/0000-0002-6054-0004
Kuldeep Verma https://orcid.org/0000-0003-0970-6440

References

Alexander, D. R., & Ferguson, J. W. 1994, ApJ, 437, 879
Allard, F., Hauschildt, P. H., Alexander, D. R., & Starrfield, S. 1997, ARA&A, 35, 137
Allard, F., Homeier, D., & Freytag, B. 2012, RSPTA, 370, 2765
Anders, E., & Grevesse, N. 1989, GeCoA, 53, 197
Andrássy, R., & Spruit, H. C. 2013, A&A, 559, A122
Andrássy, R., & Spruit, H. C. 2015, A&A, 578, A106
Angulo, C., Arnould, M., Rayet, M., et al. 1999, NuPhA, 656, 3
Anthony-Twarog, B. J., Twarog, B. A., Kaluzny, J., & Shara, M. M. 1990, AJ, 99, 1504
Asplund, M., Grevesse, N., & Sauval, A. J. 2005, in ASP Conf. Ser. 336, Cosmic Abundances as Records of Stellar Evolution and Nucleosynthesis, ed. T. G. Barnes & F. N. Bash, III (San Francisco, CA: ASP), 25
Asplund, M., Grevesse, N., Sauval, A. J., & Scott, P. 2009, ARA&A, 47, 481
Baglin, A., Auvergne, M., Barge, P., et al. 2009, in IAU Symp. 253, Transiting Planets, ed. F. Pont, D. Sasselov, & M. J. Holman (Cambridge: Cambridge Univ. Press), 71
Bahcall, J. N., Pinsonneault, M. H., & Wasserburg, G. J. 1995, RvMP, 67, 781
Baraffe, I., Chabrier, G., Allard, F., & Hauschildt, P. H. 1995, ApJL, 446, L35
Basu, S. 1997, MNRAS, 288, 572
Basu, S., & Antia, H. M. 2004, ApJL, 606, L85
Beck, P. G., Bedding, T. R., Mosser, B., et al. 2011, Sci, 332, 205
Bedding, T. R., Mosser, B., Huber, D., et al. 2011, Natur, 471, 608
Benedict, G. F., Henry, T. J., Franz, O. G., et al. 2016, AJ, 152, 141
Bergemann, M., & Serenelli, A. 2014, in Solar Abundance Problem, ed. E. Niemczura, B. Smalley, & W. Pych (Basel: Springer International), 245
Bessell, M., Bloxham, G., Schmidt, B., et al. 2011, PASP, 123, 789
Bessell, M. S. 1990, PASP, 102, 1181
Bessell, M. S., & Brett, J. M. 1988, PASP, 100, 1134
Bessell, M. S., Castelli, F., & Plez, B. 1998, A&A, 333, 231
Böhm-Vitense, E. 1958, ZAp, 46, 108
Brandt, T. D., & Huang, C. X. 2015, ApJ, 807, 24
Bressan, A., Marigo, P., Girardi, L., et al. 2012, MNRAS, 427, 127
Bressan, A. G., Chiosi, C., & Bertelli, G. 1981, A&A, 102, 25
Brocato, E., Cassisi, S., & Castellani, V. 1998, MNRAS, 295, 711
Brogaard, K., Bruntt, H., Grundahl, F., et al. 2011, A&A, 525, A2
Brogaard, K., VandenBerg, D. A., Bruntt, H., et al. 2012, A&A, 543, A106
Caffau, E., Ludwig, H.-G., Steffen, M., Freytag, B., & Bonifacio, P. 2011, SoPh, 268, 255
Caputo, F., Chieffi, A., Tornambe, A., Castellani, V., & Pulone, L. 1989, ApJ, 340, 241
Cardelli, J. A., Clayton, G. C., & Mathis, J. S. 1989, ApJ, 345, 245
Carraro, G., Villanova, S., Demarque, P., et al. 2006, ApJ, 643, 1151
Casagrande, L., Silva Aguirre, V., Schlesinger, K. J., et al. 2016, MNRAS, 455, 987
Casagrande, L., Silva Aguirre, V., Stello, D., et al. 2014, ApJ, 787, 110
Cassisi, S., Potekhin, A. Y., Pietrinferni, A., Catelan, M., & Salaris, M. 2007, ApJ, 661, 1094
Cassisi, S., & Salaris, M. 2013, Old Stellar Populations: How to Study the Fossil Record of Galaxy Formation (Weinheim: Wiley-VCH)
Cassisi, S., Salaris, M., & Irwin, A. W. 2003, ApJ, 588, 862
Castellani, V., Chieffi, A., Tornambe, A., & Pulone, L. 1985, ApJ, 296, 204
Castelli, F. 2005, MSAIS, 8, 34
Castelli, F., & Kurucz, R. L. 2004, arXiv:astro-ph/0405087
Caughlan, G. R., & Fowler, W. A. 1988, ADNDT, 40, 283
Cayrel de Strobel, G., Crifo, F., & Lebreton, Y. 1997, in ESA Special Publication 402, Hipparcos—Venice '97, ed. R. M. Bonnet et al. (Noordwijk: ESA), 687
Chabrier, G., & Baraffe, I. 2000, ARA&A, 38, 337
Chaplin, W. J., Kjeldsen, H., Christensen-Dalsgaard, J., et al. 2011, Sci, 332, 213
Chaplin, W. J., Lund, M. N., Handberg, R., et al. 2015, PASP, 127, 1038
Chen, Y., Girardi, L., Bressan, A., et al. 2014, MNRAS, 444, 2525
Choi, J., Dotter, A., Conroy, C., et al. 2016, ApJ, 823, 102
Christensen-Dalsgaard, J. 2008, Ap&SS, 316, 113
Claret, A., & Torres, G. 2016, A&A, 592, A15
Claret, A., & Torres, G. 2017, ApJ, 849, 18
Coc, A., Uzan, J.-P., & Vangioni, E. 2014, JCAP, 10, 050
Cohen, M., Wheaton, W. A., & Megeath, S. T. 2003, AJ, 126, 1090
Cordier, D., Pietrinferni, A., Cassisi, S., & Salaris, M. 2007, AJ, 133, 468
Cox, J. P., & Giuli, R. T. 1968, Principles of Stellar Structure (New York: Gordon and Breach)
Cyburt, R. H., Amthor, A. M., Ferguson, R., et al. 2010, ApJS, 189, 240
Cyburt, R. H., & Davids, B. 2008, PhRvC, 78, 064614
Degl'Innocenti, S., Prada Moroni, P. G., Marconi, M., & Ruoppo, A. 2008, Ap&SS, 316, 25
Degroote, P., Aerts, C., Baglin, A., et al. 2010, Natur, 464, 259
Delfosse, X., Forveille, T., Ségransan, D., et al. 2000, A&A, 364, 217
Demarque, P., Sarajedini, A., & Guo, X.-J. 1994, ApJ, 426, 165
Dewitt, H. E., Graboske, H. C., & Cooper, M. S. 1973, ApJ, 181, 439
Dotter, A. 2016, ApJS, 222, 8
Dotter, A., Chaboyer, B., Jevremović, D., et al. 2008, ApJS, 178, 89
Dotter, A., Sarajedini, A., & Anderson, J. 2011, ApJ, 738, 74
Feiden, G. A., & Chaboyer, B. 2012, ApJ, 757, 42
Ferguson, J. W., Alexander, D. R., Allard, F., et al. 2005, ApJ, 623, 585
Formicola, A., Imbriani, G., Costantini, H., et al. 2004, PhLB, 591, 61
Frandsen, S., Lehmann, H., Hekker, S., et al. 2013, A&A, 556, A138
Fukugita, M., Ichikawa, T., Gunn, J. E., et al. 1996, AJ, 111, 1748
Gaia Collaboration, van Leeuwen, F., Vallenari, A., et al. 2017, A&A, 601, A19
Gallart, C., Monelli, M., Mayer, L., et al. 2015, ApJL, 811, L18
Gilliland, R. L., Brown, T. M., Christensen-Dalsgaard, J., et al. 2010, PASP, 122, 131
Girardi, L., Bertelli, G., Bressan, A., et al. 2002, A&A, 391, 195

González Hernández, J. I., & Bonifacio, P. 2009, A&A, 497, 497
González-Fernández, C., Hodgkin, S. T., Irwin, M. J., et al. 2017, arXiv:1711.08805
Graboske, H. C., Dewitt, H. E., Grossman, A. S., & Cooper, M. S. 1973, ApJ, 181, 457
Gratton, R. 2000, in ASP Conf. Ser. 198, Stellar Clusters and Associations: Convection, Rotation, and Dynamos, ed. R. Pallavicini, G. Micela, & S. Sciortino (San Francisco, CA: ASP), 225
Gratton, R., Bragaglia, A., Carretta, E., & Tosi, M. 2006, ApJ, 642, 462
Gratton, R. G., Carretta, E., & Bragaglia, A. 2012, A&ARv, 20, 50
Grevesse, N., & Noels, A. 1993, in Origin and Evolution of the Elements, ed. N. Prantzos, E. Vangioni-Flam, & M. Casse, 15
Grevesse, N., & Sauval, A. J. 1998, SSRv, 85, 161
Haft, M., Raffelt, G., & Weiss, A. 1994, ApJ, 425, 222
Hammer, J. W., Fey, M., Kunz, R., et al. 2005, NuPhA, 758, 363
Hauschildt, P. H., & Baron, E. 1999, JCoAM, 109, 41
Henyey, L., Vardya, M. S., & Bodenheimer, P. 1965, ApJ, 142, 841
Huber, D., Bedding, T. R., Stello, D., et al. 2011, ApJ, 743, 143
Huber, D., Chaplin, W. J., Christensen-Dalsgaard, J., et al. 2013, ApJ, 767, 127
Husser, T.-O., Wende-von Berg, S., Dreizler, S., et al. 2013, A&A, 553, A6
Iben, I., Jr. 1975, ApJ, 196, 525
Iglesias, C. A., & Rogers, F. J. 1996, ApJ, 464, 943
Imbriani, G., Costantini, H., Formicola, A., et al. 2004, A&A, 420, 625
Itoh, N., Uchida, S., Sakamoto, Y., Kohyama, Y., & Nozawa, S. 2008, ApJ, 677, 495
Jordi, C., Gebran, M., Carrasco, J. M., et al. 2010, A&A, 523, A48
Kallinger, T., Weiss, W. W., Barban, C., et al. 2010, A&A, 509, A77
Kirby, E. N. 2011, PASP, 123, 531
Kjeldsen, H., & Bedding, T. R. 1995, A&A, 293, 87
Kopytova, T. G., Brandner, W., Tognelli, E., et al. 2016, A&A, 585, A7
Krief, M., Feigel, A., & Gazit, D. 2016, ApJ, 821, 45
Krishna Swamy, K. S. 1966, ApJ, 145, 174
Kunz, R., Fey, M., Jaeger, M., et al. 2002, ApJ, 567, 643
Kurucz, R. L. 1970, SAOSR, 309
Kurucz, R. L., Peytremann, E., & Avrett, E. H. 1974, Blanketed Model Atmospheres for Early-Type Stars (Washington, DC: Smithsonian)
Langhoff, S. R., Schwenke, D. W., & Partridge, H. 1997, in IAU Symp. 178, ed. E. F. van Dishoeck (Heidelberg: Astronomisches Rechen-Institut), 295
Lodders, K. 2010, ASSP, 16, 379
Lubin, J. B., Rodriguez, J. E., Zhou, G., et al. 2017, arXiv:1706.02401
MacDonald, J., & Mullan, D. J. 2012, MNRAS, 421, 3084
Magic, Z., Serenelli, A., Weiss, A., & Chaboyer, B. 2010, ApJ, 718, 1378
Maíz Apellániz, J. 2006, AJ, 131, 1184
Maíz Apellániz, J. 2017, arXiv:1711.10919
Mamajek, E. E., Torres, G., Prsa, A., et al. 2015, arXiv:1510.06262
Marigo, P., & Aringer, B. 2009, A&A, 508, 1539
Mészáros, S., Allende Prieto, C., Edvardsson, B., et al. 2012, AJ, 144, 120
Miglio, A., Brogaard, K., Stello, D., et al. 2012, MNRAS, 419, 2077
Monelli, M., Martínez-Vázquez, C. E., Bernard, E. J., et al. 2016, ApJ, 819, 147
Montalbán, J., Miglio, A., Noels, A., et al. 2013, ApJ, 766, 118
Moore, K., & Garaud, P. 2016, ApJ, 817, 54
Mosser, B., Barban, C., Montalbán, J., et al. 2011, A&A, 532, A86
Munakata, H., Kohyama, Y., & Itoh, N. 1985, ApJ, 296, 197
Origlia, L., Valenti, E., Rich, R. M., & Ferraro, F. R. 2006, ApJ, 646, 499
Percival, S. M., & Salaris, M. 2003, MNRAS, 343, 539
Percival, S. M., Salaris, M., Cassisi, S., & Pietrinferni, A. 2009, ApJ, 690, 427
Perryman, M. A. C., Brown, A. G. A., Lebreton, Y., et al. 1998, A&A, 331, 81
Pietrinferni, A., Cassisi, S., & Salaris, M. 2010, A&A, 522, A76
Pietrinferni, A., Cassisi, S., Salaris, M., & Castelli, F. 2004, ApJ, 612, 168
Pietrinferni, A., Cassisi, S., Salaris, M., & Castelli, F. 2006, ApJ, 642, 797
Pietrinferni, A., Cassisi, S., Salaris, M., & Hidalgo, S. 2013, A&A, 558, A46
Pietrinferni, A., Cassisi, S., Salaris, M., Percival, S., & Ferguson, J. W. 2009, ApJ, 697, 275
Piotto, G., Milone, A. P., Bedin, L. R., et al. 2015, AJ, 149, 91
Potekhin, A. Y. 1999, A&A, 351, 787
Rauer, H., Aerts, C., Cabrera, J. & PLATO Team 2016, AN, 337, 961
Rauer, H., Catala, C., Aerts, C., et al. 2014, ExA, 38, 249
Reimers, D. 1975, MSRSL, 8, 369
Ricker, G. R., Winn, J. N., Vanderspek, R., et al. 2014, Proc. SPIE, 9143, 914320
Rogers, F. J., & Nayfonov, A. 2002, ApJ, 576, 1064
Röser, S., Schilbach, E., Piskunov, A. E., Kharchenko, N. V., & Scholz, R.-D. 2011, A&A, 531, A92
Salaris, M., & Cassisi, S. 2015, A&A, 577, A60
Salaris, M., & Cassisi, S. 2017, RSOS, 4, 170192
Salaris, M., Cassisi, S., Pietrinferni, A., Kowalski, P. M., & Isern, J. 2010, ApJ, 716, 1241
Sandquist, E. L. 2004, MNRAS, 347, 101
Saumon, D., Chabrier, G., & van Horn, H. M. 1995, ApJS, 99, 713
Schwenke, D. W. 1998, FaDi, 109, 321
Serenelli, A., Weiss, A., Cassisi, S., Salaris, M., & Pietrinferni, A. 2017, A&A, 606, A33
Serenelli, A. M., Basu, S., Ferguson, J. W., & Asplund, M. 2009, ApJL, 705, L123
Siess, L., Dufour, E., & Forestini, M. 2000, A&A, 358, 593
Silva Aguirre, V., Basu, S., Brandão, I. M., et al. 2013, ApJ, 769, 141
Silva Aguirre, V., Bojsen-Hansen, M., Slumstrup, D., et al. 2017, arXiv:1710.09847
Silva Aguirre, V., Davies, G. R., Basu, S., et al. 2015, MNRAS, 452, 2127
Simon, M., & Toraskar, J. 2017, ApJ, 841, 95
Spada, F., Demarque, P., Kim, Y.-C., Boyajian, T. S., & Brewer, J. M. 2017, ApJ, 838, 161
Stancliffe, R. J., Fossati, L., Passy, J.-C., & Schneider, F. R. N. 2015, A&A, 575, A117
Stassun, K. G., Feiden, G. A., & Torres, G. 2014, NewAR, 60, 1
Tayar, J., Somers, G., Pinsonneault, M. H., et al. 2017, ApJ, 840, 17
Taylor, B. J. 2006, AJ, 132, 2453
Taylor, B. J., & Joner, M. D. 2005, ApJS, 159, 100
Thoul, A. A., Bahcall, J. N., & Loeb, A. 1994, ApJ, 421, 828
Tognelli, E., Prada Moroni, P. G., & Degl'Innocenti, S. 2011, A&A, 533, A109
Torres, G., Andersen, J., & Giménez, A. 2010, A&ARv, 18, 67
Trampedach, R., Stein, R. F., Christensen-Dalsgaard, J., Nordlund, Å, & Asplund, M. 2014, MNRAS, 445, 4366
Twarog, B. A., Ashman, K. M., & Anthony-Twarog, B. J. 1997, AJ, 114, 2556
Valle, G., Dell'Omodarme, M., Prada Moroni, P. G., & Degl'Innocenti, S. 2016, A&A, 587, A16
VandenBerg, D. A., Bergbusch, P. A., Ferguson, J. W., & Edvardsson, B. 2014, ApJ, 794, 72
Verma, K., Faria, J. P., Antia, H. M., et al. 2014, ApJ, 790, 138
Vernazza, J. E., Avrett, E. H., & Loeser, R. 1981, ApJS, 45, 635
Viallet, M., Meakin, C., Prat, V., & Arnett, D. 2015, A&A, 580, A61
Villanova, S., Geisler, D., Carraro, G., Moni Bidin, C., & Muñoz, C. 2013, ApJ, 778, 186
Villante, F. L. 2010, ApJ, 724, 98
Vinyoles, N., Serenelli, A. M., Villante, F. L., et al. 2017, ApJ, 835, 202
Weiss, A., Serenelli, A., Kitsikis, A., Schlattl, H., & Christensen-Dalsgaard, J. 2005, A&A, 441, 1129
Westera, P., Lejeune, T., & Buser, R. 1999, in ASP Conf. Ser. 192, Spectrophotometric Dating of Stars and Galaxies, ed. I. Hubeny, S. Heap, & R. Cornett (San Francisco, CA: ASP), 203
Westera, P., Lejeune, T., Buser, R., Cuisinier, F., & Bruzual, G. 2002, A&A, 381, 524
White, T. R., Bedding, T. R., Stello, D., et al. 2011, ApJ, 743, 161
Windmiller, G., Orosz, J. A., & Etzel, P. B. 2010, ApJ, 712, 1003
Wood, T. S., Garaud, P., & Stellmach, S. 2013, ApJ, 768, 157
Zasowski, G., Johnson, J. A., Frinchaboy, P. M., et al. 2013, AJ, 146, 81